NUMERICAL INVESTIGATION OF HYDROGEN UNDER-EXPANDED JET FLOW CONSIDERING VISCOUS EFFECTS

Farbod Vakilimoghaddam

A Thesis

In the Department

of

Mechanical and Industrial Engineering

Presented in Partial Fulfillment of the Requirements

For the Degree of Master of Applied Science (Mechanical Engineering) at

Concordia University

Montreal, Quebec, Canada

December 2016

CONCORDIA UNIVERSITY

School of Graduate Studies

This is to certify that the thesis prepared

By: **Farbod Vakilimoghaddam**

Entitled: **Numerical Investigation of Hydrogen Under-Expanded Jet Flow Considering Viscous Effects**

and submitted in partial fulfillment of the requirements for the degree of

MASTER OF APPLIED SCIENCE (MECHANICAL ENGINEERING)

Complies with the regulation of the University and meets the accepted standards with respect to originality and quality.

Signed by the final Examining Committee:

_____	Chair
Dr.Rolf Wüthrich	
_____	Examiner
Dr. S. Samuel Li	
_____	Examiner
Dr. Charles Basenga Kiyanda	
_____	Thesis Supervisor
Dr. Marius Paraschivoiu	

Approved by: _____

Chair of Department or Graduate Program Director

____/____/____ _____

Dean of Faculty

ABSTRACT

NUMERICAL INVESTIGATION OF HYDROGEN UNDER-EXPANDED JET FLOW CONSIDERING VISCOUS EFFECTS

Farbod Vakilimoghaddam

Hydrogen is the simplest and the most plentiful element in the universe. It is the cleanest burning fuel with water as the only by-product of the combustion process. Nevertheless, the low energy density per volume of hydrogen requires highly pressurized tanks to store a reasonable amount of energy. Highly pressurized storage tanks increase the risk of tank valve failure and hydrogen release into atmosphere.

In this study, two approaches are developed to investigate sudden hydrogen release. In the first approach, an analytical method is used to analyze the time histories of stagnation properties inside the chamber and sonic properties at the throat. In the second approach, computational fluid dynamics (CFD) analysis is conducted using Ansys CFX solver. Unsteady 3D Navier-Stokes equations along with an additional transport equation are the governing equations of the flow. This CFD analysis is second order accurate in time and space. The SST k-ω turbulence model is employed to study the turbulent properties of the flow. Peng-Robinson real gas EOS is used for the accurate prediction of the hydrogen properties. A fully structured high quality mesh is constructed with y^+ values under unity. This approach enables us to resolve the boundary layer with high accuracy.

The vast majority of the previous researches solved the Euler equations which neglect the fluid viscosity. In the current study, fluid viscosity is considered and the effect of boundary layer on the flow is investigated. Two storage tank pressures of $10\ MPa\ and\ 70 MPa$ are examined. It is found that the actual throat section where the flow reaches the sonic condition occurs before the pipe exit and the flow condition is supersonic at the pipe exit. A higher tank pressure leads to a smaller boundary layer thickness and therefore to a smaller supersonic flow at the exit.

ACKNOWLEDGMENTS

I would like to thank my thesis supervisor and mentor, Dr. Marius Paraschivoiu, for all his support and guidance throughout the research.

I would like to thank the Concordia Institute for Water, Energy and Sustainable Systems (CIWESS) and the Natural Sciences and Engineering Research Council of Canada (NSERC) for partial funding of this project through the Collaborative Research and Training Experience (CREATE) program.

Finally, I would like to thank my loving parents, Hossein Vakili and Soheila Sadri, for their unconditional love and support at my most challenging times. I am forever grateful to them and I would like to dedicate my thesis to my family.

TABLE OF CONTENTS

LIST OF FIGURES

LIST OF TABLES

LIST OF SYMBOLS

a	Speed of sound
A_n	Throat surface area
A_0	Constant of Beattie-Bridgeman equation of state
b	Constant of Beattie-Bridgeman equation of state
B_0	Constant of Beattie-Bridgeman equation of state
c	Constant of Beattie-Bridgeman equation of state
C_v	Specific heat of the real gas at constant volume
C_P	Specific heat of the real gas at constant pressure
$\widetilde{C_v}$	Specific heat of the ideal gas at constant volume
$\widetilde{C_P}$	Specific heat of the ideal gas at constant pressure
D	Diameter of release area
E	Total internal energy
f	State equation
h	Enthalpy
H	Total enthalpy
i	Internal energy
M	Molecular mass of hydrogen
P	Pressure
R	Gas constant
s	Entropy
u	x-component of velocity
v	y-component of velocity
w	z-component of velocity
x	x-direction of Cartesian coordinate
y	y-direction of Cartesian coordinate
z	z-direction of Cartesian coordinate
V	Magnitude of velocity vector

v	Specific volume
v^0	Specific volume at temperature T and pressure of 10^5 Pa
t	time
T	Temperature
Z	Compressibility factor

Greek Letters

α	Constant of Beattie-Bridgeman equation of state
δ	Small change
μ	Dynamic viscosity
Ψ	Total volume of the chamber
γ	Ratio of specific heats for ideal gas condition
ρ	Density

Subscripts

i	Partial derivative with respect to internal energy
v	Partial derivative with respect to specific volume
P	Partial derivative with respect to density
n	Property at the throat
t	Stagnation property
T	Partial derivative with respect to temperature

Abbreviations

CFL	Courant-Friedrichs Lewy
CFD	Computational fluid dynamics
CNG	Compressed natural gas
DNS	Direct numerical simulation
ILES	Implicit Large Eddy Simulation
LES	Large Eddy Simulation
PIV	Particle image velocimetry
RANS	Reynolds averaged Navier-Stokes
EOS	Equation of state

CHAPTER 1

INTRODUCTION

1.1 Global Warming and Renewable Energies

Human activity since the industrial revolution has increased the amount of greenhouse gases in the atmosphere. Burning fossil fuels such as coal, oil and gas are dramatically increasing concentrations of greenhouse gases in the atmosphere. Deforestation is another part of human activity which is contributing to the increase in the amount of greenhouse gases.

Average global temperature has climbed 1.4 degrees Fahrenheit (0.8 degree Celsius) around the world since 1880. Small changes in the average temperature translate into huge adverse effects on the whole planet.

Most ecosystems are affected by higher atmospheric carbon dioxide levels, combined with higher global temperatures. Extinction of many species and reduced diversity of ecosystems are the effects of global warming. For Instance, increases in atmospheric CO2 concentrations have led to an increase in ocean acidity. Increase in the amount of dissolved CO2 in the oceans increases ocean acidity and harmfully influences the living creatures in the oceans.

Ice melting and sea level rise are another outcome of global warming. Glaciers and mountain snows are rapidly melting. The sea level rise since 1993 has been estimated to have been on average 2.6 mm per year.

Today, fossil fuels are the main energy sources for the industries, transportation, and power generation. Combustion of the fossil fuels produces air pollutants and 90% of the greenhouse gas emissions come from the combustion of the fossil fuels.

Renewable energy is generally defined as energy obtained from the resources which are naturally replenished on a human timescale. According to REN21 2016 report, renewable resources

contribute to 19.2% to human's global energy consumption in 2014. Over the last decade, renewable electricity generation capacity has grown at a rapid pace and this trend is expected to continue. International organizations and industry associations forecast a wider deployment of renewable technologies around the globe. The International Energy Agency (IEA) forecasts that the renewable energy share in global electricity generation is estimated to rise to 25 percent of gross power generation in 2018.

According to Brower et al. [1] , renewable power capacity which is installed globally at the end of the year 2014 reached 1560 GW, which is almost two times higher than the 895 GW at the start of year 2004. Worldwide investments in renewable technologies amount for more than US$286 billion in 2015, with countries like China and United States heavily investing in these technologies.

Renewable energy resources exist over wide geographical areas, in contrast to the fossil fuels which are concentrated in limited number of countries. Some places around the world like Iceland and Norway, generate all their electricity using renewable energy sources. Many other countries have set the goal to reach 100% renewable energy in the future. For instance, Denmark is one of the countries which set the goal to gain all the energy from renewable resources by 2050 [2] .

Canada has an abundance of renewable resources that can be used to produce energy and is a world leader in the production and use of energy from renewable resources [3]. In Canada, hydroelectricity is the largest renewable energy source accounting for approximately 60 percent of Canada's electricity generation [3] . Wind energy is the second most important in Canada which accounts for 3.5 per cent of electricity generation.

1.2 Hydrogen: Replacement for Fossil Fuels

Hydrogen is the simplest and most plentiful element in the universe. The Hydrogen atom consists of only one proton and one electron. It is estimated that 90% of the visible universe is composed of hydrogen.

Despite its simplicity and abundance, hydrogen doesn't occur naturally on earth and it is always combined with other elements. Hydrogen is locked up in enormous quantities in water, hydrocarbons, and other organic matters. One of the challenges of using hydrogen comes from being able to effic ntly extract hydrogen from these compounds.

Hydrogen is recognized as a promising clean and renewable energy source and is the first candidate to replace petroleum and to eliminate our dependence on petroleum.

The US. Energy department [4] reported that the amount of greenhouse gases emissions per mile of the running vehicles using different fuels. Conventional vehicles which are running on gasoline produce 410 grams of greenhouse gases per mile. These conventional vehicles can be producing 320 grams of greenhouse gases, if they run on natural gas.

An incredible reduction in the amount of greenhouse gas emissions is obtained by hydrogen fueled vehicles. Hydrogen combustion in internal engines of the vehicles is clean and with zero emissions. Hydrogen running vehicles can offer the best opportunity for reducing the greenhouse gas emissions (GHC) and dependence on petroleum fuels.

Water vapor is the only combustion product of hydrogen which is environmental friendly. Hydrogen has been used for propulsion of spacecraft. NASA has used liquid hydrogen since the 1970s to propel space shuttles and other rockets into orbit. Combustion of hydrogen and oxygen generate power and produces clean water as a side product which the crew can drink.

1.3 Hydrogen Running Vehicles with Zero Emission

Today, due to environmental concerns and the urge of developing renewable energy sources to reduce our reliance on hydrocarbons and fossil fuels, efforts have been made to expand hydrogen usage as an alternative source of energy to power our transportation vehicles.

A hydrogen vehicle is a vehicle that uses hydrogen as its onboard fuel. The power plant of such vehicles converts the chemical energy of hydrogen into mechanical energy either by burning in the internal combustion engine or by reaction of hydrogen and oxygen in the fuel cell to power the electric motors.

Buses, trains, cars, motorcycles, ships, airplanes, submarines, rockets etc. are all vehicles that can be running on hydrogen fuel. Figure 1-1 shows a zero-emission hydrogen fuel cell car available in the market today.

Figure 1-1: Toyota Mirai: Zero emission hydrogen fuel cell car

Hydrogen can be used directly in the internal combustions engines. The cars with hydrogen internal combustion engines burn hydrogen in the same manner that they burn gasoline. The main diff rence is the exhaust product. Gasoline combustion products are carbon dioxide and water

vapor. Carbon dioxide is harmful to our environment. On the other hand, the only combustion product of hydrogen is water vapor which is environmentally friendly.

According to BMW hydrogen vehicle data sheet [5] , internal combustion engines which run on hydrogen have 8% higher effic ncy than gasoline engines. The hydrogen running engines have maximum efficiency of around 38%.

Fuel cells are electrochemical power generation devices in which hydrogen and oxygen are combined in the fuel cell to generate electricity, heat and water. Fuel cells can be compared to the batteries which both convert the energy from chemical reactions into electric power. Most of the fuel cells require high purity hydrogen. Impurities would quickly degrade the life of the fuel cell.

Th re are three hydrogen cars publicly available now in the market: Toyota Mirai, Hyundai ix35 FCEV and Honda Clarity.Th Toyota Mirai, was launched in japan at the end of 2014. This car has a range of 502 Km and takes about five minutes to refill [6].

BMW hydrogen 7 is a limited production of hydrogen internal combustion engine vehicles built by German automobile manufacturer, BMW. The engine is designed to allow combustion of hydrogen as well as gasoline, which makes it a bivalent engine. Unlike many other current hydrogens powered vehicles which use fuel cell technology to produce electricity to power the vehicle, BMW hydrogen 7 burns hydrogen in an internal combustion engine. In BMW hydrogen 7, hydrogen is stored in a large (170 liter) highly insulated tank in liquid form rather than as a compressed gas, which based on the BMW company offers 75% more energy per volume [5]. To keep hydrogen in the liquid state, hydrogen must be super cooled and maintained at cryogenic temperatures, at warmest, $-253\ C$. The tank is highly insulated to keep heat transfer to ambient to a bare minimum.

Extensive researches are in progress to use hydrogen as a fuel to power vehicles. Researchers are aiming to improve hydrogen related technologies and find ways to exploit potential energy of hydrogen for use in vehicles in an economically viable manner.

1.4 Hydrogen Storage Systems

Hydrogen has low energy per volume. This hydrogen property urges us to design storage systems which can store enough amount of hydrogen.

Hydrogen storage system design is an important parameter in the hydrogen industry. One of the challenging and crucial steps for advancing hydrogen applications is the development of safe, reliable, effi ent and effective storage systems.

There are three different hydrogen storage systems:

- High pressure gaseous storage;
- Liquid hydrogen storage;
- Material based storage.

The first two technologies are more mature than the last technology. The material based storage is largely under development and is highly dependent on the development of the advanced materials.

The high pressure gaseous hydrogen storage system is currently the most popular and widely used method for hydrogen storage. Currently, over 80% of total 215 refueling stations operating world-wide uses high pressurized hydrogen storage systems [7] . The major advantage of this technology is the simplicity.

High amount of energy is required for the hydrogen liquefaction process. This process involves pressurizing and cooling steps, which is of high energy consumption. The liquid hydrogen is in a cryogenic state and boils at $20.268\ K$ $(-252.882\ C)$. These tanks should be well insulated to minimize the heat transfer between the tank and the surroundings to prevent and minimize the evaporation and boil-off.

Material based storage method is at preliminary stages of research. In this method, hydrogen atoms are bounded with other elements and other materials. There are two bonding mechanism in this technology, adsorption and absorption, which are described in details in [8] .

1.5 Hydrogen Safety

Hydrogen has one of the widest explosive\ignition mix range with air. This means that the mixture of air and hydrogen, even with small fraction of hydrogen, will most likely lead to an explosion. This feature of hydrogen and air mixture makes safety issues a big concern for its application.

It should be mentioned that this mixture burns in the ultraviolet color range which is invisible to naked human eyes. Hence, flame detectors are essential for most of the hydrogen usages to identify if the hydrogen leakage is burning.

According to the hydrogen accidental database, 60% of the accidental hydrogen release led to ignition with no apparent reason. The hydrogen auto ignition is an interning topic for the researchers According to some of the studies the molecular diffusiv ty is a potential cause of these auto ignitions.

The discussed issues with the hydrogen mixture make hydrogen storage systems a challenging part of the hydrogen industry. Furthermore, the low energy per volume feature of hydrogen urge us to store hydrogen at high pressures which increase the risk of tank valve failure and of hydrogen release.

1.6 Objectives

The low energy density per volume of hydrogen requires highly pressurized tanks to store a reasonable amount of energy. These pressurized storage tanks increase the risk of tank valve failure and hydrogen release into the atmosphere.

The objective of this work is to investigate the flow behavior of the sudden hydrogen release from pressurized tanks when considering viscous flows and turbulence effects.

The specific objectives of this work are:

- To solve unsteady compressible Navier-Stokes equations considering the flow viscosity;
- To investigate the fictitious converging diverging nozzle formed by boundary layers;
- To study the flow behavior near the exit region;
- To investigate the release from tanks with diff rent initial storage conditions.

1.7 Literature Review of Hydrogen Release

In this section, a review of the literature related to the hydrogen release is provided.

Zhang et.al. [9] reviewed hydrogen related technologies development over the past decade. This paper provides a survey on different hydrogen storage systems, hydrogen production and associated electricity generation technologies.

Compressed natural gas and compressed hydrogen energy content per mole are compared by Wallace [10]. They concluded that natural gas stored at 20.78 MPa contains five times as much energy as hydrogen stored under the same conditions.

A large number of works [11]–[13] have been made to investigate the thermophysical properties of hydrogen gas.

Analytical model describing the isentropic expansion of a real gas from a high-pressure chamber are introduced by Johnson [14] and [15] . Johnson [15] applied these models to tabulate sonic and stagnation properties of nitrogen and helium at pressures up to 30 MPa. In this thesis, the same algorithm is applied to a diff rent equation of state to derive the thermodynamic relations and develop an analytical model.

Mohamed et al. [16] studied hydrogen release from a high pressure storage tank to investigate the real gas effects of hydrogen at high pressures. They developed a 3-D unstructured tetrahedral finite volume Euler solver to numerically simulate the hydrogen release. This solver is modified to consider the real gas effects. The modifications required to calculate the real gas Jacobian matrices and eigenvectors as well as to obtain the Roe's averaged convective fluxes are described in this work. They concluded that employment of real gas model for the calculation of high pressure hydrogen properties is essential.

Khaksarfard et al. [17] numerically simulated the release of hydrogen in the near jet area with real gas models. Flow viscosity was neglected in their study and Euler equations were the governing equations of the fluid flow. They concluded that for the initial tank pressure of $P_0 = 70\ MPa$ the ideal gas assumption under-estimates the release velocity by almost 20% which implies the necessity of implementing real gas models for high storage pressures.

K. Nasrifar [18] investigated eleven diff rent equation of states for prediction of thermodynamic properties of hydrogen. They concluded that the Peng Robinson EOS gives the most accurate results.

Markert et al. [19] compared a number of equation of states to predict hydrogen release properties from diff rent storage tanks. They concluded that the ideal gas assumption is not accurate for high pressures and low temperatures. According to their simulations, the Peng Robinson model is the most accurate real gas equation for hydrogen release applications.

Nagao et al.[20] investigated the effect of different equation of states (EOS) on the critical nozzle coeffic nt of discharge. They concluded that the coeffic nt of discharge decreases by increasing the Reynolds number. The $k-\varepsilon$ turbulence model was employed to study the turbulent features of the flow. They stated that the coeffic nt of discharge is decreased as the real gas effects become stronger. The analysis is performed under steady state conditions. The total pressure and total temperature inlet boundary conditions were specified and the hydrogen storage tank was not simulated in their model.

Kubo et al.[21] investigated the choking phenomena of the convergent nozzle flow, experimentally. They used four convergent nozzles with the same diameter followed by a straight pipe with variable lengths. They stated that in the case when the back-pressure ratio is larger than the choking pressure ratio, the main flow Mach number at the nozzle exit is larger than unity and the flow has is supersonic.

Yoshimaru et al. [22] numerically and experimentally investigated the under-expanded gaseous flow through a straight micro-tube. The micro-tube used in their studies is $495\mu m$ in diameter and $56.3mm$ in length. They reported supersonic conditions of the flow at the pipe exit.

Lijo et al.[23] investigated the choking phenomena inside the straight pipe, numerically. Their simulations were performed under steady state conditions. They used the $k-\omega$ model for turbulence modelling. The hydrogen storage had an initial tank temperature of $T_0 = 300$ K and initial tank pressure of $P_0 = 101$ kPa . The outlet pressure varied between 80 kPa to 20 kPa . Their results showed that boundary layer thinning leads to sonic conductance upstream of the pipe exit.

Hamzehloo et al. [24] used an LES model to study the near-nozzle shock structure and mixing characteristics of highly turbulent under-expanded hydrogen jets. They simulated nozzle pressure

ratios of 8.5,10,30 and 70 . The geometry of the Mach disk, reflected shock waves and turbulent shear layers were studied. They reported supersonic conditions at the nozzle exit.

Afroosheh et al. [25] investigated the hydrogen release from a high-pressure hydrogen storage tank using LES turbulence model to predict the turbulent features of the flow. The developed numerical code is equipped with wiggle detectors to reduce the contribution of the upwinding part in the flux calculations and to reduce the undesired artificial viscosity which is added to the solution by the upwind methodology. Performance and stability of the developed numerical tool is reported in their studies. They concluded that Euler simulations are less accurate for the hydrogen release application but more conservative in safety aspects because they predict higher mass flow rate and higher temperatures.

Chernyavsky et al. [26] investigated the physics of hydrogen release from compressed storage vessels for flow conditions corresponding to a subsonic turbulent jet venting into the atmosphere at a Mach number ~ 0.3 using LES and particle image velocimetry (PIV) measurements. A major focus of the work is the investigation of the dynamic features of the flow and mixing processes by analyzing the detailed instantaneous data available from LES.

Accidental hydrogen release and dispersion were studied experimentally by Ganci et al. [27] . They studied release from a 1 MPa hydrogen storage tank through a 11mm orifice in a pipeline. They have investigated the effect of wind direction on the cloud shape. The hydrogen mass concentration, as a function of distance from the release hole, was reported in their study.

The hydrogen release from storage tank in a cryogenic state is studied by Venetsanos et al. [28] using homogeneous equilibrium model (HEM). The flow structure of the highly under-expanded jets are further explored in [29]–[31].

Merilo et al. [32] investigated the potential safety hazard associated with a hydrogen fuel-cell vehicle in a garage. A series of tests examined the risk involved with hydrogen release and deflagration in a structure built to simulate a one-car garage. Pressures within the garage were measured by four pressure transducers mounted on the inside walls of the garage. These experiments examined the effectiveness of different ventilation techniques to reduce the hydrogen concentration in the enclosure.

The dispersion characteristics of hydrogen leaking through a small hole were investigated numerically and experimentally by Han et al. [33] . They explored the safety distances from hydrogen stations. The leak holes of $0.5, 0.7\ and\ 1.0$ mm in diameters and the release pressures of $100, 200, 300$ and 400 bar were studied.

CFD simulations of hydrogen release in an underground parking lot and in a multistory parking garage are also carried out in [34], [35].

Physics of spontaneous ignition of high-pressure hydrogen release is explored by Bragin et al. [36]. They used LES to study the ignition dynamics in a tube with a non-inertial rupture disk separating the high-pressure hydrogen storage and the atmosphere. They reported that because of stagnation conditions, a chemical reaction first commences in the tube boundary layer and subsequently propagates throughout the tube cross-section.

The spontaneous ignition of hydrogen is also investigated by Xu et al. [37]. The mixture-averaged multi component approach is used for the calculation of the molecular transport. They stated a possible mechanism for spontaneous ignition through molecular diffusion.

Panda et al. [38] investigated the ignition and flame characteristics of the under-expanded cryogenic hydrogen jets, experimentally. In their experiments, a non-intrusive laser spark focused on the jet axis was used to measure the maximum ignition distance.

Hydrogen self-ignition and explosion during discharge from a high-pressure chamber are further investigated in [39]–[42].

1.8 Thesis Outline

This section presents a brief description and key points of each chapter in this dissertation.

- Chapter 2: Governing Equations and Numerical Setup

  Governing equations of the fluid flow which are the unsteady compressible Navier-Stokes equations with an extra transport equation are introduced. Next, turbulence model is presented as a closure to the system of equations. Numerical schemes used for time and space discretizations and the numerical setup of the CFD model are provided. The applied real gas equation of state is discussed. Finally, the analytical model for the sudden hydrogen release is developed based on real gas equation of state. This analytical model is used to validate the computational analysis.

- Chapter 3: Numerical Simulation

  The computational domain, the computational grid and the boundary layer meshing are presented. Next, boundary conditions and initial conditions of the CFD analysis are introduced.

- Chapter 4: Numerical Validation

  The validation of the current computational analysis is performed using two diff rent approaches. First the results of the CFD model is compared with an analytical model described in chapter 2. Second, the results of the current study are compared with a former study in the literature.

- Chapter 5: Results

  Th results of the CFD analysis are provided in this chapter. First, the flow structure of the highly under expanded jet flow is discussed. Then, the fictitious converging-diverging nozzle formed by the boundary layer is explored. This fictitious nozzle is revealed to be the reason for the flow supersonic condition at the pipe exit. Next, the evolution of the flow properties inside the pipe is presented. Later, different initial storage tank pressures and temperatures are investigated. Finally, the mass flow rate of hydrogen release from the tank is studied.

CHAPTER 2

GOVERNING EQUATIONS AND NUMERICAL SETUP

2.1 Governing Equations

Unsteady compressible Navier-Stokes equations are the governing equations of the fluid flow under consideration. The conservation equations of mass, momentum and energy are as follows [43] :

$$\frac{\partial \rho}{\partial t} + \nabla . (\rho \vec{u}) = 0 \qquad (2\text{-}1)$$

$$\frac{\partial (\rho \vec{u})}{\partial t} + \nabla . (\rho \vec{u} \otimes \vec{u}) = -\nabla \mathrm{P} + \nabla . \tau \qquad (2\text{-}2)$$

$$\frac{\partial (\rho h_{tot})}{\partial t} - \frac{\partial P}{\partial t} + \nabla . (\rho \, \vec{u} \, h_{tot}) = \nabla . (\lambda \ \nabla \mathrm{T}) + \nabla . (\vec{u} . \tau) \qquad (2\text{-}3)$$

where $\vec{u}$ is the velocity vector, μ is the dynamic viscosity, τ is stress tensor, ρ is density, P is pressure and h_{tot} is the total enthalpy.

Soon after hydrogen release into air, the mixture of hydrogen and air exists in the flow. The transport equation is applied to find the concentration of the diff rent components in the mixture. This equation determines how the components of the fluid are transported within the fluid. The transport equation is documented in Ansys CFX document [43] .

Reynolds decomposition is the approach behind construction of the Reynolds averaged Navier-Stokes equations. The instantaneous flow properties in the Navier-Stokes equations can be decomposed into time averaged and fluctuating components. The instantaneous flow velocity and flow pressure is decomposed into these components in the following:

$$u_i = \overline{U}_\iota + u_i' \tag{2-4}$$

$$p_i = \overline{P}_\iota + p_i' \tag{2-5}$$

where $u_i \; and \; p_i$ are the instantaneous velocities and pressure components, $\overline{U}_\iota \; and \; \overline{P}_\iota$ are the time averaged velocity and pressure components and $u_i' \; and \; p_i'$ are the fluctuating components. The subscripts $i = 1,2 \text{ and } 3$ refer to each of the components in the X, Y and Z directions, respectively.

Averaging the Navier-Stokes equations and using the above-mentioned decomposition leads to the RANS equations. Simulation of the RANS equations is generally adopted for practical engineering calculations and greatly reduces the computational cost comparing to the Large Eddy Simulation (LES) and the Direct Numerical Simulation (DNS).

The averaging procedure in the RANS equations introduces additional unknown terms containing products of the fluctuating quantities. These terms are called Reynolds stresses and need to be modeled by additional equations of known quantities to achieve closure in the system of equations. Closure implies that there are enough equations for all the unknowns. The closure is achieved by turbulence models which provide models for the Reynolds stresses. The RANS equations are available in [43] .

Based on the Boussinesq approximation, the Reynolds stress can be expressed as a product of eddy viscosity , μ_t and local mean flow rate [43].

$$-\rho\overline{u_j{}'u_\iota{}'} = \mu_t\left(\frac{\partial U_i}{\partial x_j} + \frac{\partial U_j}{\partial x_i}\right) - \frac{2}{3}\delta_{ij}\left(\rho k + \mu_t\frac{\partial U_k}{\partial x_k}\right) \tag{2-6}$$

2.2 Turbulence Modelling

Turbulence is a chaotic and irregular flow regime in which flow properties such as velocity, pressure, temperature show random variation with respect to time and space.

Two equation shear stress transport (SST) k − ω turbulence model is used for the current CFD study. The SST k − ω is developed by Menter [44] to blend the robust and accurate formulation of k-ω in the near wall region and k-ε model for the free stream flow .

The $k-\varepsilon$ model is ideal for predicting free flow behavior away from walls. The $k-\omega$ model is suitable for simulating flow near the walls. The SST k − ω model combines the benefits of these models which enable us to capture all the features of the flow near the wall and in the free flow region.

The SST k-ω turbulence model introduces two extra transport equations for turbulent kinetic energy (k) and turbulent frequency (ω). These transport equations are as follows [43] :

$$\frac{\partial}{\partial t}(\rho k)+\frac{\partial}{\partial x_j}(\rho k u_j)=\frac{\partial}{\partial x_j}\left(\Gamma_k\frac{\partial k}{\partial x_j}\right)+\widetilde{G_k}-Y_k+S_k \qquad (2\text{-}7)$$

$$\frac{\partial}{\partial t}(\rho \omega)+\frac{\partial}{\partial x_j}(\rho \omega u_j)=\frac{\partial}{\partial x_j}\left(\Gamma_\omega\frac{\partial \omega}{\partial x_j}\right)+G_\omega-Y_\omega+D_\omega+S_\omega \qquad (2\text{-}8)$$

where $\widetilde{G_k}$ represents the generation of turbulence kinetic energy due to mean velocity gradients, G_ω is the generation of ω . Y_k and Y_ω are the dissipation of k and ω due to the turbulence. D_ω is the cross-diffusio term, S_ω and S_k are the source terms. The rest of the equations of this turbulence model are available in [43].

2.3 Numerical Setup

The computational analysis of the hydrogen release is performed using the commercial ANSYS CFX software. Unsteady Compressible 3D Navier-Stokes equations with an additional transport equation are solved to simulate the flow.

The under-expanded hydrogen jet is a complex fluid flow containing number of shocks and discontinuities. For the advection term of the Navier-Stokes equations, a high-resolution scheme is implemented. This scheme exhibits Total Variation Diminishing (TVD) characteristic to avoid spurious and non-physical oscillations where shocks and discontinues are present. This approach is second order accurate in space.

For the time discretization, second order implicit backward Euler method is applied. Implicit methods are computationally much more expensive than explicit methods and it is harder to implement. Implicit methods calculate the state of the system by solving a system of equations involving the current desired state and the previous ones.

The CFL condition is an essential consideration for solving partial diff rential equations, numerically. According to the CFL condition, the time step size should be smaller than a certain value to have a stable solution. The maximum CFL number for explicit methods is usually of the order of unity. Implicit methods are stable for much higher CFL numbers but depends how is the nonlinearity of the problem.

An adaptive time step method is implemented in this model, which automatically determines the time step size based on the truncation error associated with the time integration scheme. Adjustment of the time step size is made by comparing the truncation error with the desired level of accuracy. If the truncation error is smaller than a specified tolerance, the size of the time step is increased; if the truncation error is greater, the time step size is decreased [43]. The convergence criteria is set to $1e-5$ in the simulations and the adjustments to the time step sizes are made based on this value. The initial time step for the simulations is $10^{-9}s$. The time step change factor limits the degree to which the time step size can be changed at each time step. CFX default values are used for the time step change factor [43].

Figure 2-1 shows the time step size effects on the Mach number distribution along the pipe centerline. The current CFD model is stable even for very high CFL numbers of 85, but increasing the time step sizes generate some erroneous and inaccurate results. In the current study, the maximum time step size is limited to 10^{-8} s, which leads to maximum courant number of 8.5 to be able to resolve the transient details with high accuracy.

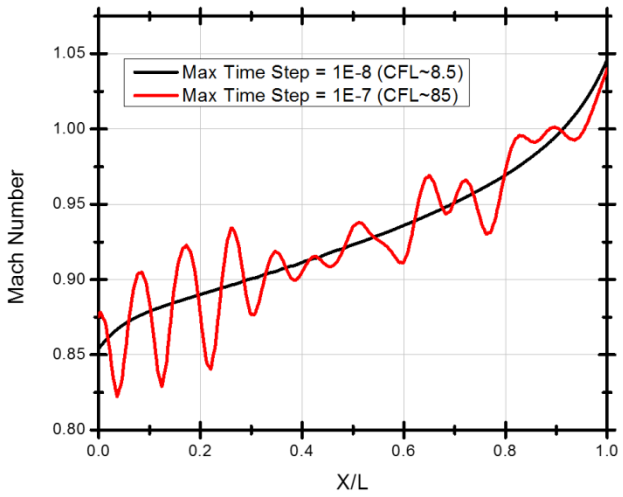

Figure 2-1: Time step size effects on the Mach number distribution along the pipe centerline

The simulations are performed on a cluster of 12 cores with 2.67 GHz processing frequency. With the specified maximum CFL number in the solution, the simulations take around 120 hours to complete 100μs of the release.

2.4 Real Gas Model

Accurate predictions of high pressure hydrogen properties require a real gas model. The Peng Robinson model is used as a real gas equation of state in this study. This model gives pressure as a function of temperature and volume as following [43]:

$$P = \frac{RT}{v-b} - \frac{a(T)}{v^2 - 2bv + b^2} \quad (2\text{-}9)$$

where:

$$a(T) = a_0(1 + n(1 - \sqrt{\frac{T}{T_c}}))^2 \quad (2\text{-}10)$$

$$a_0 = \frac{0.4572\, R^2\, {T_c}^2}{P_c} \quad (2\text{-}11)$$

$$b = \frac{0.0778\, R\, T_c}{P_c} \quad (2\text{-}12)$$

$$n = 0.37464 + 1.5422\omega - 0.26993\omega^2 \quad (2\text{-}13)$$

Some of the hydrogen properties are as follows:

Hydrogen Properties	
Critical temperature	32.98 [k]
Molar mass	2.016 [$\frac{Kg}{Kmol}$]
Critical pressure	12.93 [bar]
Critical volume	64.20 [$\frac{Cm^3}{mol}$]
Acentric factor (ω)	-0.217
Boiling temperature	20.27 [k]

Table 2-1: Hydrogen properties

For calculation of specific heat capacity , a forth order polynomial with the following coeffic nt is employed [43]:

$$C_p = a_1 + a_2 T + a_3 T^2 + a_4 T^3 + a_5 T^4 \qquad (2\text{-}14)$$

a_1	$a_2\ [K^{-1}]$	$a_3\ [K^{-2}]$	$a_4\ [K^{-3}]$	$a_5\ [K^{-4}]$
2.883	3.681	-0.772	0.692e-8	-0.213e-11

Table 2-2 : Th polynomial coefficients for calculation of hydrogen specific heat capacity

Kinetic theory model is used for calculation of dynamic viscosity and thermal conductivity.

2.5 Analytical Model

In this chapter an analytical model, developed by Mohamed et al. [16], is used to study the hydrogen sudden release from a high-pressure storage tank. In this model, time histories of the stagnation and sonic properties are calculated.

Hydrogen is initially stored in a high-pressure chamber and exits through an orifice to atmospheric air. Schematic diagram of the control volume is shown in the following figure:

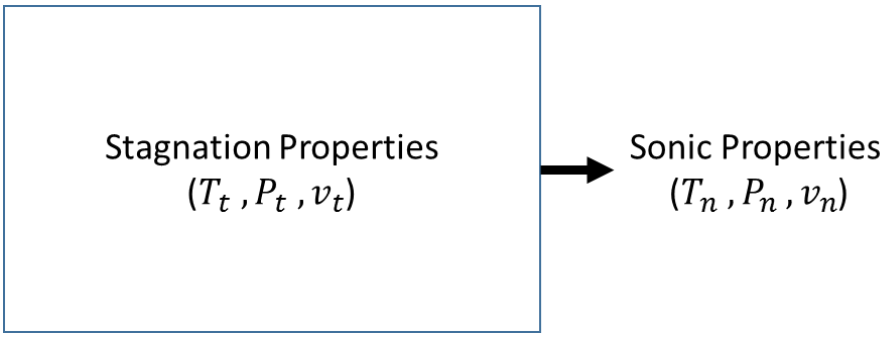

Figure 2-2: Schematic diagram of the control volume [16]

A control volume approach is used to develop this analytical model and to obtain time histories of thermodynamic properties at two specific locations:

- Stagnation properties inside the chamber;
- Sonic properties at the throat.

The thermodynamic behavior of hydrogen at high pressures deviates from predicted properties by ideal gas law. Deviation between ideal gas and real gas assumptions become bigger for hydrogen storages with higher pressures. The ideal gas assumption is not accurate enough to analyze the release from a high-pressure storage tank. Therefore, real gas equation of state is used to derive all the thermodynamic relations and properties.

Following assumptions are made to develop the code and simulate the hydrogen release [16] :

1- The flow properties are uniformly distributed inside the chamber.
2- The flow is choked at the throat and flow velocity is equal to local speed of sound.
3- Expansion of the flow occurs from the stagnation state inside the chamber to the sonic state at the throat. Quasi one dimensional isentropic flow is considered to model the expansion
4- Hydrogen remains at the gaseous phase throughout the process.
5- Expansion of the hydrogen from the stagnation state inside the chamber to the critical state at the orifice takes place in small region near the orifice.

The release process of the high-pressure hydrogen consists of two major steps:

- Isentropic expansion;
- Adiabatic release.

In the first stage, isentropic expansion, flow isentropically expands from the stagnation stat inside the chamber to the sonic state at the throat. The flow properties of the isentropically expanded flow are calculated to obtain corresponding sonic properties at the throat for each stagnation state inside the chamber.

In the second stage, adiabatic release, the conservation of mass and energy equations are integrated to get the new stagnation state inside the chamber.

The conservation equations, thermodynamic relations and the algorithm which the analytical code is based on are all described in details in the APPENDIX A.

CHAPTER 3

NUMERICAL SIMULATION

3.1 Computational Domain

Figure 3-1 shows the computational domain with the applied boundary conditions. The domain consists of two zones: a high pressure hydrogen storage tank and air.

The hydrogen releases from the high-pressure chamber into the atmospheric downstream region. These two chambers are connected via a straight pipe with constant area. The straight pipe has an inner diameter of 1 mm and axial length of L=2 mm ($L/D = 2$). The cylindrical air containing chamber has a radius of $r = 15mm$ $(15D)$ and a length of $L = 22mm$ $(22D)$.

To reduce the computational cost of the simulations, a slice of the geometry is modeled and symmetric boundary conditions are applied on the side walls to represent the whole 360 degree of the geometry. Two slices of 5 and 10 degrees are simulated and the comparison between these two slices shows very close results For this study, the 10-degree slice is chosen to conduct the simulation.

In order to confirm that the axisymmetric consideration does not restrict certain eddy sizes and provide accurate results , the results of 10 degree slice simulation is compared with Afroosheh et.al. [25] which simulated a full geometry without axisymmetric consideration. The comparison of the results which is presented in section 4.2 shows that the results of these two studies are in good agreement and axisymmetric consideration is valid.

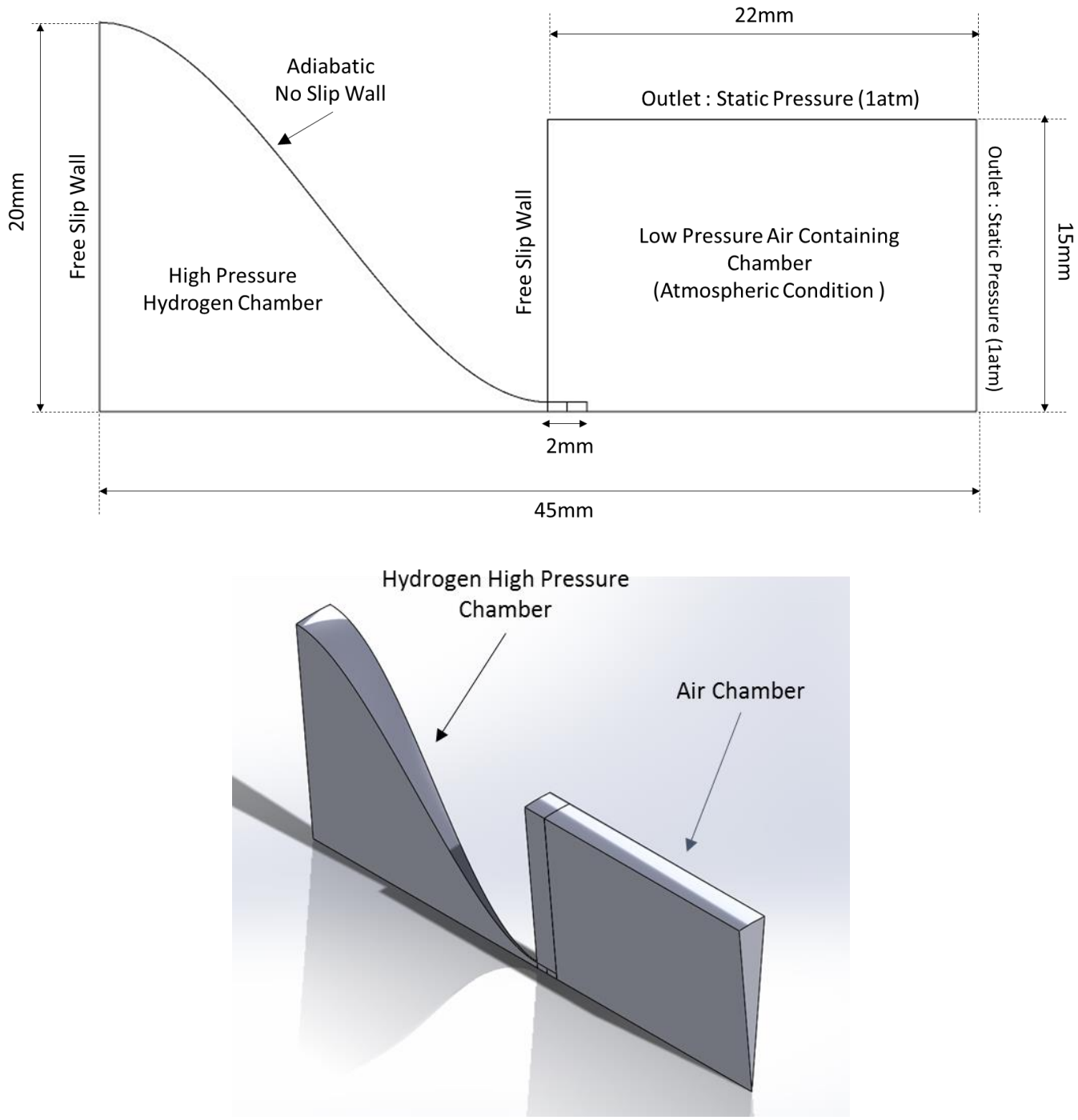

Figure 3-1: Computational domain with applied boundary conditions

The geometry of the chamber is designed to be smooth to prevent any sudden jumps and steps in the geometry and adverse effects on the results in the pipe. For that purpose, a 4^{th} order polynomial is used to model the hydrogen tank body. The volume of hydrogen chamber is $V = 51.79\ \mathrm{mm}^3$.

In order to ensure free development of the flow without any constraints, the left side wall of the air containing chamber is moved 2 mm away from the pipe exit. This approach not only ensures free evolution of the flow but also makes the boundary condition applied at the wall further away from the region of interest. The further the boundary condition is applied from the regions of interest, higher solution accuracy is achieved.

3.2 Computational Grid

3.2.1 Mesh Characteristic

In the current computational analysis, a fully structured mesh is constructed with hexahedral type elements. These elements are highly space effic nt. In addition, the accuracy of the solution with these elements is the highest among all types of mesh elements.

The changes in size of the elements are smooth without any sudden jumps in size. Smoothness is an important factor for preventing erroneous results. In the current study, the elements growth ratio is 1.1 which leads to slow transition and smoothness and ultimately a high-quality mesh.

Fine meshes are generated for the regions with high gradients in flow properties. Th high gradients occur in the straight pipe and near the exit region. Coarser elements are generated for the regions with lower gradient in flow properties.

Ansys Meshing software is used to generate the computational grid. The mesh characteristics are provided in the following table:

Mesh Characteristic	
Number of elements	1.2 million
Number of inflation layers	30
Elements growth ratio	1.1
y^+	Less than unity

Table 3-1 : Mesh characteristics

Figure 3-2 shows the computational grid. A closer look into the straight pipe and near the exit region with high gradients of the flow is illustrated in Figure 3-2 (b).

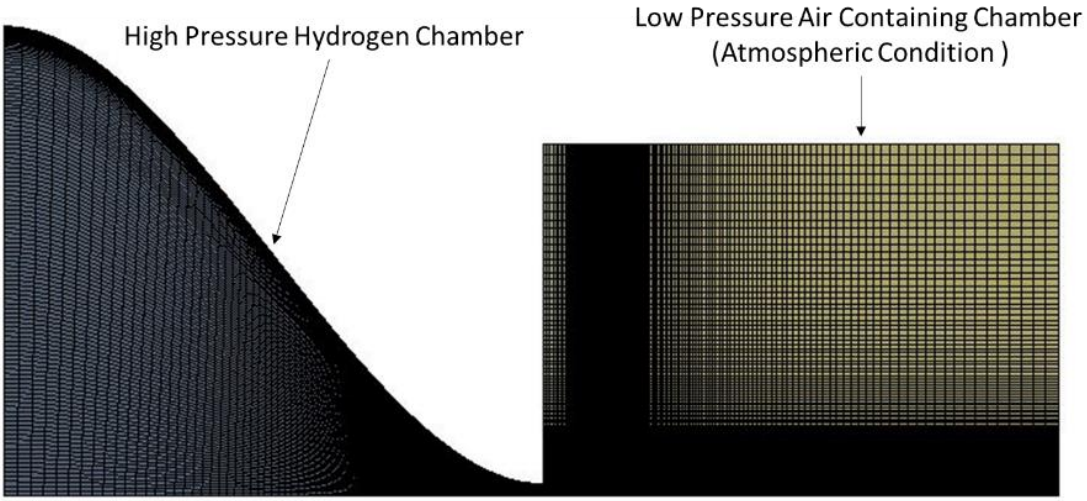

(a)

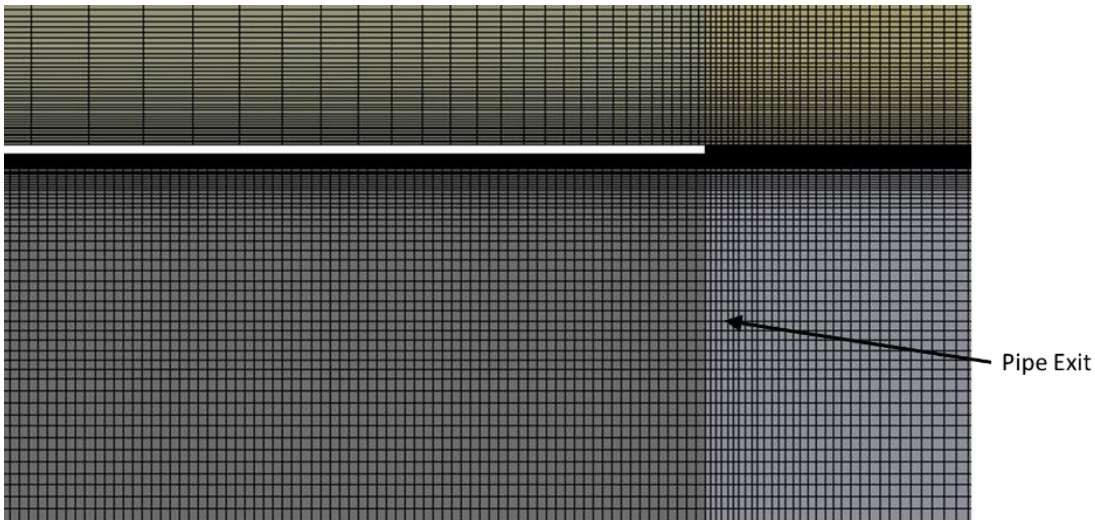

(b) closer look into the near exit region

Figure 3-2: Computational grid

3.2.2 Boundary Layer Meshing

The flow near the wall is complex and large gradients in the flow properties occur in the wall normal direction and it is important to capture these gradients accurately. Applying sufficiently fine elements inside the boundary layer is a critical component for proper computational analysis.

The y^+ value is an important parameter to properly construct the mesh inside the boundary layer. It allows us to determine whether our first cell resides within the viscous sub-layer or the logarithmic region. Two approaches exist to resolve the boundary layer. First, using wall function and second, resolving without use of wall functions. The distance of the first node from the wall identifies which approach is taken for the boundary layer. If the first node is sufficiently close to the wall, in a way that gives y^+ value under unity, no wall function is required to resolve the boundary layer.

In the current computational analysis, the first node is sufficiently close to the adjacent wall with y^+ value of less than unity. The first cell is located inside the viscous sub-layer and no wall function is required to solve the boundary layer. This approach gives a solution with high accuracy because no extra approximation is made to solve the flow.

The number of inflation layers used to solve the boundary layer is 30 and the growth ratio in the size of elements inside the boundary layer is 1.1.

To ensure proper resolution of the turbulent boundary layer, the eddy viscosity ratio is analyzed in the post processing section. This investigation proves the adequate number of prism layers to fully capture the turbulent boundary layer profile. The eddy viscosity ratio is defined as:

$$\text{Eddy Viscosity Ratio} = \frac{\text{Turbulent Eddy Viscosity}}{\text{Dynamic Viscosity}} \qquad (3\text{-}1)$$

By plotting this variable and superimposing the mesh in the near-wall region, the boundary layer resolution is visualized. The eddy viscosity ratio visualization inside the straight pipe is illustrated in *Figure 3-3*. The eddy viscosity ratio shows the level of turbulence in the flow. Higher ratio is an indication of higher turbulent viscosity and higher turbulence in the flow.

Since we have prescribed a y^+ of less than unity, the first cell resides inside the viscous sub-layer which exhibits laminar flow characteristics with no turbulent viscosity. As we gradually move through the buffer region and into the logarithmic region, a large rise in the viscosity ratio is seen before it dissipates into the free stream. The maximum value of the eddy viscosity ratio occurs in the middle of the boundary layer. This visualization also gives us an indication of the physical boundary layer thickness. Twice the location of the maximum eddy viscosity ratio is the boundary layer edge where turbulent viscosity is zero.

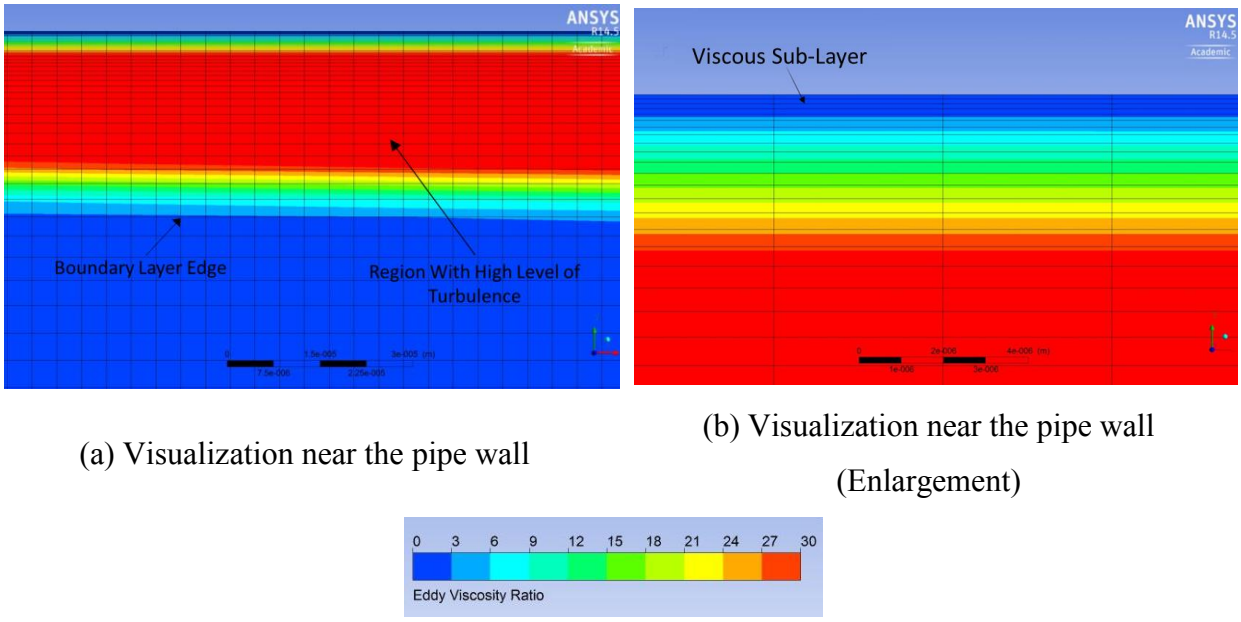

(a) Visualization near the pipe wall

(b) Visualization near the pipe wall (Enlargement)

Figure 3-3: Th eddy viscosity ratio visualization inside the release pipe

These visualizations show how well the boundary layer mesh is constructed and ultimately how well the boundary layer profile is resolved.

3.2.3 Grid Convergence Study

Grid convergence study is an essential part of the computational analysis. The purpose of this study is to confirm that the refinement of the mesh does not affect the results significantly.

Two computational grids with 1.2 and 1.8 million elements are constructed. The areas of refinements are the zones with high gradient of the flow properties which includes the straight pipe and near the nozzle exit region. The growth ratio of 1.1 is kept the same and more layers are used for the grid with 1.8 million elements.

It is important to note that for all the generated grids, regardless of refinement, the distance of the first cell away from the wall is the same. This is done to conserve and maintain $y^+$and to make sure that the variation in results does not originate from turbulence modelling assumptions.

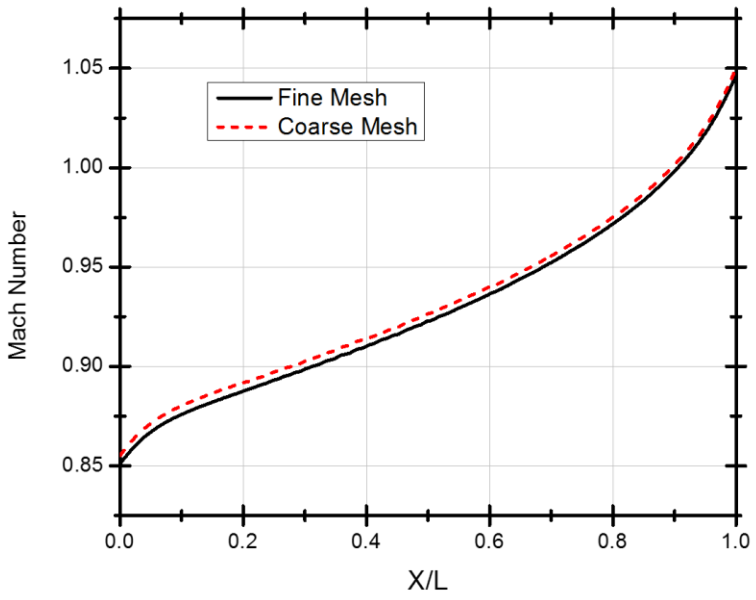

Figure 3-4: Grid convergence study: Th flo Mach number distribution along the pipe centerline

Figure 3-4 shows the Mach number distribution along the pipe centerline for two computational grids at the specific time of t=50μs after the release for the tank with initial tank temperature and pressure of $T_0 = 300$ K and $P_0 = 10$ MPa. The maximum error between the two meshes is less than 1%. Therefore, the grid with 1.2 million elements is chosen to perform the simulations.

3.3 Boundary Conditions

No slip wall boundary condition is applied to the straight pipe walls and the hydrogen tank body. Application of this boundary condition forces the fluid to have a zero velocity at the solid wall.

Symmetric boundary conditions are applied to the side walls. This boundary condition imposes constrains that mirrors the flow on either side of the plane. Static pressure is set as the boundary condition for the right side and the upper side of the air containing chamber. It should be noted that all the walls are adiabatic with no heat transfer with the surrounding environment.

Boundary conditions are specified at far distances to have the least adverse impact on the flow properties inside the regions of interest. The right side of the air chamber is 22mm (22D) and the left side wall of the air chamber is 2mm (2D) away from the straight pipe exit. The top side of the air chamber is 15 mm (15D) away of the pipe exit.

3.4 Initial Conditions

The fluid properties are assumed to be uniformly distributed throughout the computational domain, initially. Initial velocity of the flow is zero which implies quiescence state. The air containing chamber has atmospheric conditions for all the simulations ($T_0 = 300$ K and $P_0 = 1$ atm).

Figure 3-5 shows the initial hydrogen mass fraction throughout the domain. The mass fraction value of unity signifies pure hydrogen and mass fraction of zero signifies pure air in the mixture. The initial contact surface is located at 1 mm $(1D)$ upstream of the pipe exit in the middle of the straight pipe.

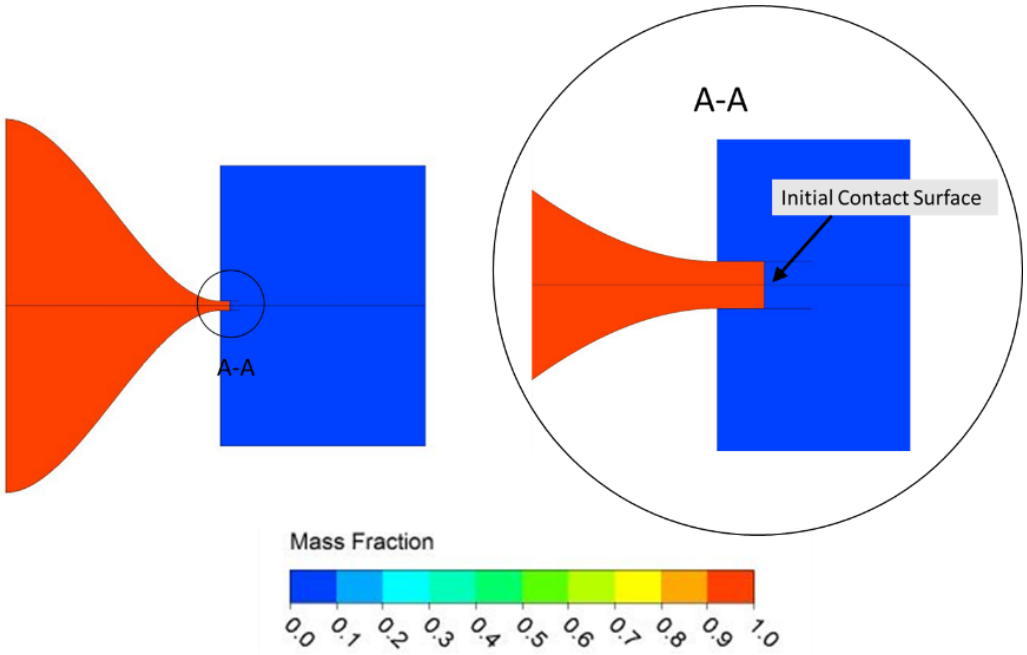

Figure 3-5: Initial mass concentration

In the current study, release of hydrogen from storage tanks with initial tank pressures of $P_0 = 10$ *and* 70 MPa and initial tank temperature of $T_0 = 300$ K *and* $T_0 = 200$ K are investigated.

CHAPTER 4

NUMERICAL VALIDATION

In this chapter, the validation of the CFD analysis is conducted using two diff rent approaches. First, the choked flow analytical model, described in section 2.5. Second, the results of the current CFD analysis are compared with former finding in the literature.

4.1 Comparison with the Choked Flow Analytical Solution

In the previous chapter, an analytical model is used to study the sudden release from a high-pressure hydrogen storage tank. In this model, time histories of the stagnation and sonic properties are calculated. The release properties (sonic properties at the throat) which are calculated using the analytical model is used for validation of the CFD model. *Table 4-1* presents release properties of the flow for the case with initial tank pressure and temperature of $P_0 = 10$ MPa , $T_0 = 300$ k respectively using two different approaches. Th results correspond to $t = 50\mu s$ after the release.

	$Release\ Density$ (kg/m3)	$Release\ Pressure$ (MPa)	$Release\ Temperature$ (k)
Analytical model	5.06	5.26	246.34
CFD simulations	5.0	5.1	247

Table 4-1: Th hydrogen release properties; Validation of the CFD model

The diff rences between the analytical and computational analysis for release density, release pressure and release temperature are 1.2%, 3% and 0.26%, respectively. It can be concluded that the results of these two approaches are in good agreement with each other and accuracy of the CFD model is verified.

4.2 Comparison with Former Findings in the Literature

In addition to the above-mentioned comparison with the analytical solution, the simulation results are compared with previous work in the in the literature. Afroosheh et al. [25] developed an in-house code using mixed finite element – finite volume scheme on an unstructured tetrahedral mesh to investigate the hydrogen release from high pressure storage tank. The LES turbulence model is employed to investigate the turbulent features of the flow. The finite element technique is used for diffusive fluxes, while for convective fluxes, a finite volume integration is applied. A second order implicit scheme is implemented for the temporal term. The convective fluxes are discretized with the 2nd order Roe-MUSCL (βγ scheme) while a second order finite element method is used for the diffusive fluxes. The subgrid scale terms are modeled by the Smagorinsky model. The Iterative GMRES solver is used for solving the system of equations.

The numerical simulation conducted by Afroosheh et al. [25] is compared with the experimental results obtained by Chernyavsky et al. [26]. Chernyavsky et al. [26] have studied the physics of hydrogen release from compressed storage vessels for flow conditions corresponding to a subsonic turbulent jet venting into atmosphere at a Mach number ~ 0.3. Particle image velocimetry (PIV) measurements were used in their studies. They investigated the dynamic features of the flow and mixing processes during the transient process. The results of the numerical simulation performed by Afroosheh et al. [25] are in good agreement with the experimental results of the Chernyavsky et al. [26] .

Figure 4-1 and Figure 4-2 present the comparison between the current CFD study and Afroosheh et al. [25] study, for the case with initial tank pressure of $P = 10MPa$ and initial tank temperature of $T = 300\ K$ at $t = 15\ \mu s$ after the release. The flow Mach number and mass concentration along the centerline are explored.

The comparison between the two studies shows good agreement in the results. The locations of Mach disk, contact surface and bow shock are predicted the same in both studies. The Mach disk strength is predicted higher in the current study, which is expected to be due to the mesh sizes. In the current study, a much finer mesh is applied to capture the flow features. The axisymmetric boundary condition applied to the side walls of the geometry enabled us to generate this fine mesh.

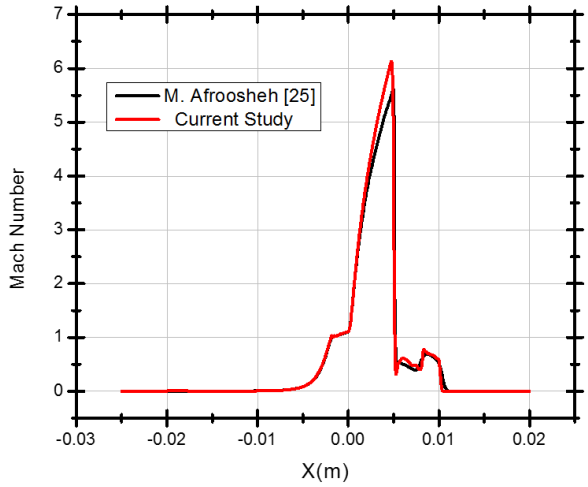

Figure 4-1 : Mach number distribution along the centerline ; Comparison between the current CFD study and Afroosheh et al. [25]

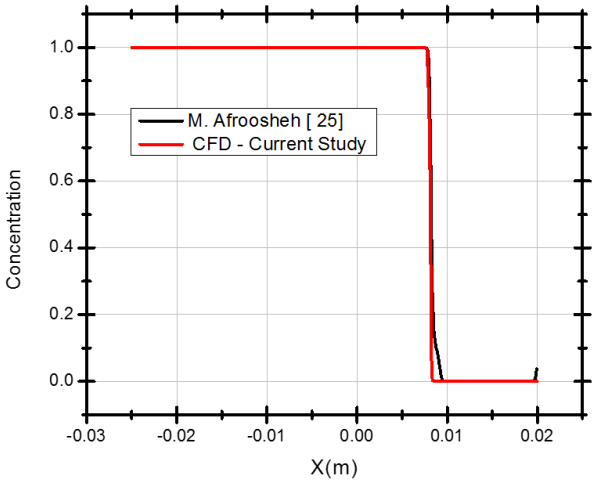

Figure 4-2: Mass concentration distribution along the centerline ; Comparison between the current CFD study and Afroosheh et al. [25]

CHAPTER 5

RESULTS

Computational analysis of the hydrogen release from high pressure storage tanks is conducted using Ansys CFX commercial software and the results are provided in this chapter. Two storage tank pressures of $P_0 = 10\text{MPa}$ and $P_0 = 70\text{MPa}$ are explored.

The vast majority of the work in the literature investigated the under expanded hydrogen release without considering the flow viscosity. The flow viscosity is neglected in their studies because of high speed of the flow. Euler equations are the governing equations for their simulations. In this work, compressible Navier-Stokes equations with considerations of viscous terms are solved to analyze the hydrogen release from the high-pressure storage tanks.

Accurate simulation of high pressure hydrogen release requires real gas equations of states. Real gas effects become stronger for high pressures. In this work, the Peng-Robinson EOS is used as a real gas model to accurately predict the properties of the flow during the release.

5.1 The Flow Structure

5.1.1 Under-Expanded Jet Flow

In this section, the highly under expanded jet flow structure is discussed.

Figure 5-1 shows concentration, temperature, Mach number and density field contours for hydrogen release from a storage tank with initial tank pressure and temperature of $P_0 = 10\text{MPa}$ and $T_0 = 300$ K at t=15μs after the release.

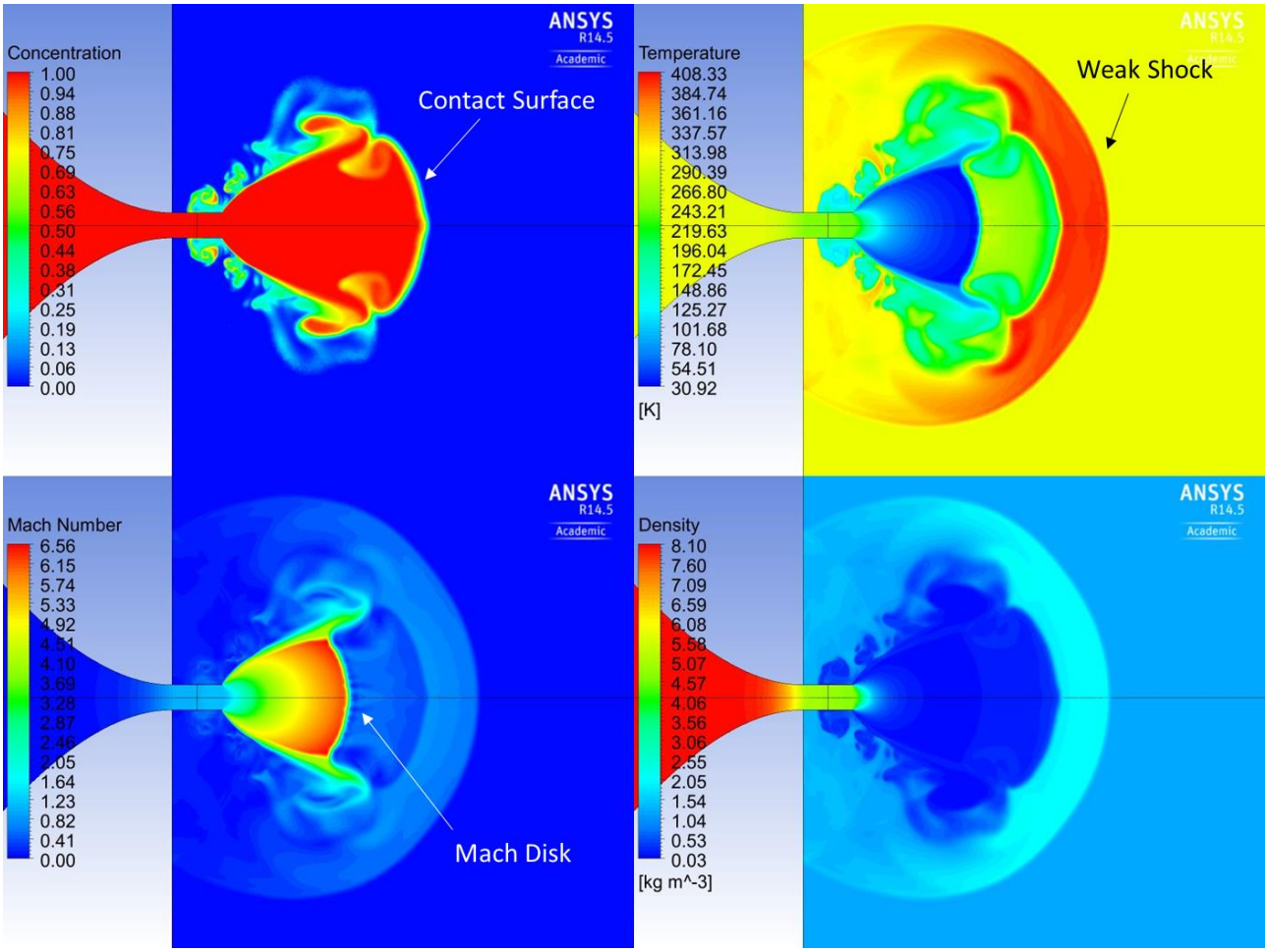

Figure 5-1: Th flow properties contour at t=15 μs after the release

The jet propagates at supersonic speed into the atmosphere and a strong shock wave which is known as the Mach disk is formed downstream of the release area. The Mach disk is a very strong normal shock which is perpendicular to the direction of the flow. This normal shock is in the area where the hydrogen concentration is 100%. Passing through this normal shock causes the temperature of the flow to increase and the flow Mach number to decrease significantly. The flow upstream of this shock wave is supersonic with the Mach number much greater than unity. The flow conditions change to subsonic by passing through the Mach disk and the Mach number becomes lower than unity. Upstream of the Mach disk in the supersonic region, flow is at cryogenic state; extremely low temperatures.

Downstream of the Mach disk, a weaker shock wave is located which is known as a lead shock. This shock is formed ahead of the hydrogen jet where hydrogen concentration is 0%. The flow temperature decreases across the interface of this shock wave into the ambient temperature and the flow downstream of this shock is not affected by the jet formation. Since the lead shock is a much weaker shock than the Mach disk, it is also called a weak shock.

The contact surface is the interface of hydrogen and air in the flow. The flow experience slight increase in the Mach number by passing through the contact surface. It should be mentioned that the flow conditions, upstream and downstream of this interface are both subsonic and the flow Mach number is below unity. The flow temperature increases significantly across this interface. The highest flow temperatures occur in the region between the contact surface and the lead shock.

The lateral shock is the shock formed in a lateral direction. Across this shock, flow experiences a jump in temperature from cryogenic state (extremely low temperatures) into the ambient temperatures.

To provide a better understanding of the flow structure and the changes in the flow properties across these shocks and discontinuities, the flow properties along the centerline are plotted in Figure 5-2.

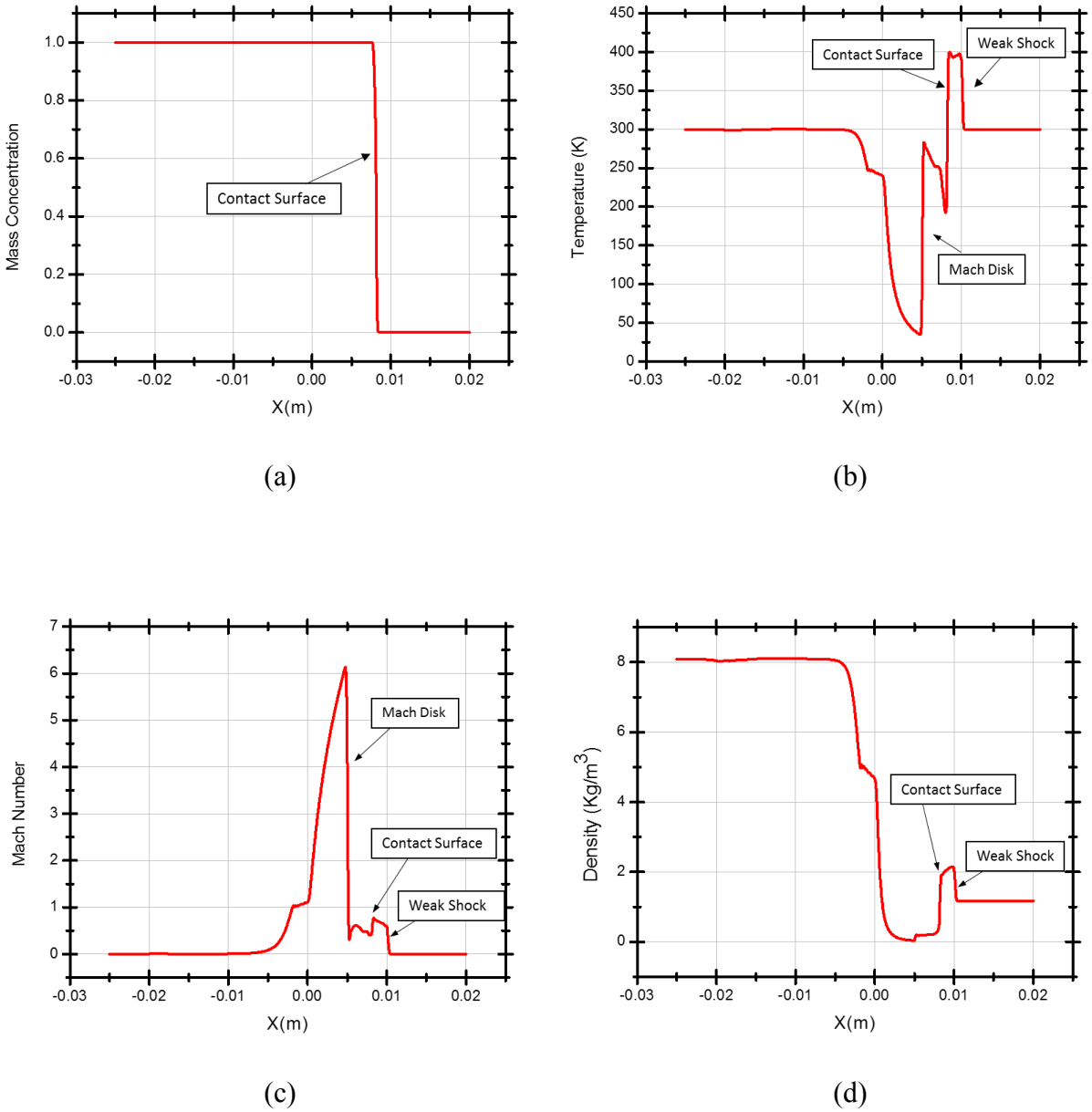

Figure 5-2: Th flow properties along the centerline at t=15μs after the release

According to Figure 5-2-c the flow accelerates along the flow direction and the Mach number increases until it reaches the Mach disk downstream of the release area. As mentioned earlier, the Mach disk is a very strong normal shock with a high gradient of the flow properties across. The flow upstream of the Mach disk is highly supersonic and the Mach number is much higher than unity whilst after passing this shock flow condition is changed to subsonic. Slight increase in the Mach number is seen further downstream at the contact surface of hydrogen and air. It should be noted that the flow condition after this slight increase remains subsonic and the flow Mach number is less than unity. The flow Mach number experiences a sudden decrease at the lead shock. The air, downstream of the weak shock is not affected by the formation and presence of the hydrogen jet.

The flow temperature decreases along the centerline and it reaches its lowest value upstream of the Mach disk. The flow temperatures are extremely low in this region and the flow has cryogenic condition. Downstream of the Mach disk, a decreasing trend in the flow temperature is seen until it reaches the contact surface. The flow temperature increases significantly at the contact surface and reaches its maximum value. The flow downstream of the weak shock is not affected by the formation of hydrogen jet.

The hydrogen density inside the high-pressure chamber is much higher than the ambient air density. The flow density decreases along the centerline until it reaches the Mach disk. The flow density is slightly increased across the Mach disk and remains almost the same until it reaches the contact surface, where a significant increase in density is observed. As mentioned earlier, the ambient air downstream of the weak shock is not affected by the formation of the hydrogen jet.

Schematic diagram of near nozzle structure of an under expanded jet flow [30] is shown in *Figure 5-3*-a. The flow Mach number field distribution contour for the current CFD study at t=15μs after the release is presented in *Figure 5-3*-b.

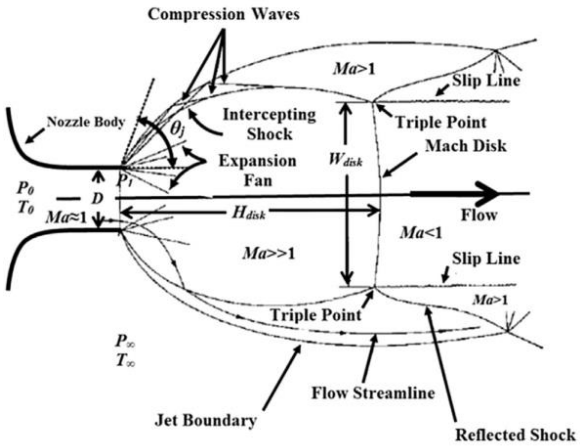

(a)

Schematic diagram of near nozzle structure of under-expanded jets [30]

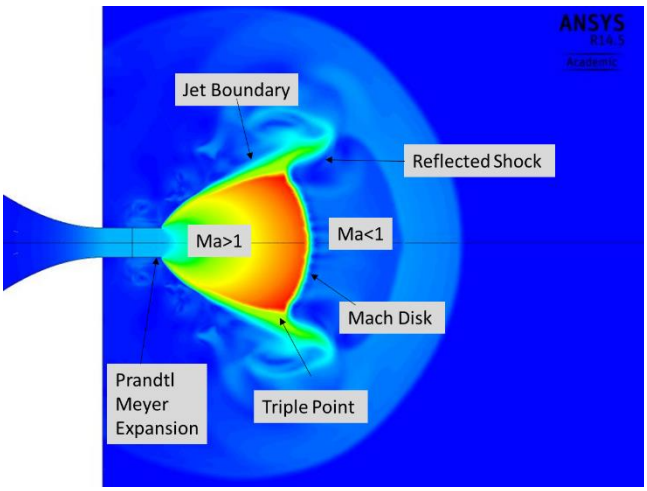

(b)

Mach number contour distribution ; current CFD study

Figure 5-3: Th flo structure of the highly under expanded jet flo

Th flow structure which is predicted by the current CFD analysis is in perfect agreement with the expected flow structure of the highly under expanded jets which is provided in the literature and all the flow features are well captured in the current study.

The under expanded jet flow is complex and includes many shocks and discontinuities with high gradients in the flow properties which requires a very stable code with high quality mesh to capture all the flow features.

Figure 5-4 shows the flow local speed of sound contour for the case with initial tank pressure of $P_o = 10$ MPa and temperature of $T_o = 300$ K . The results correspond to the specific time of t=15μs after the release.

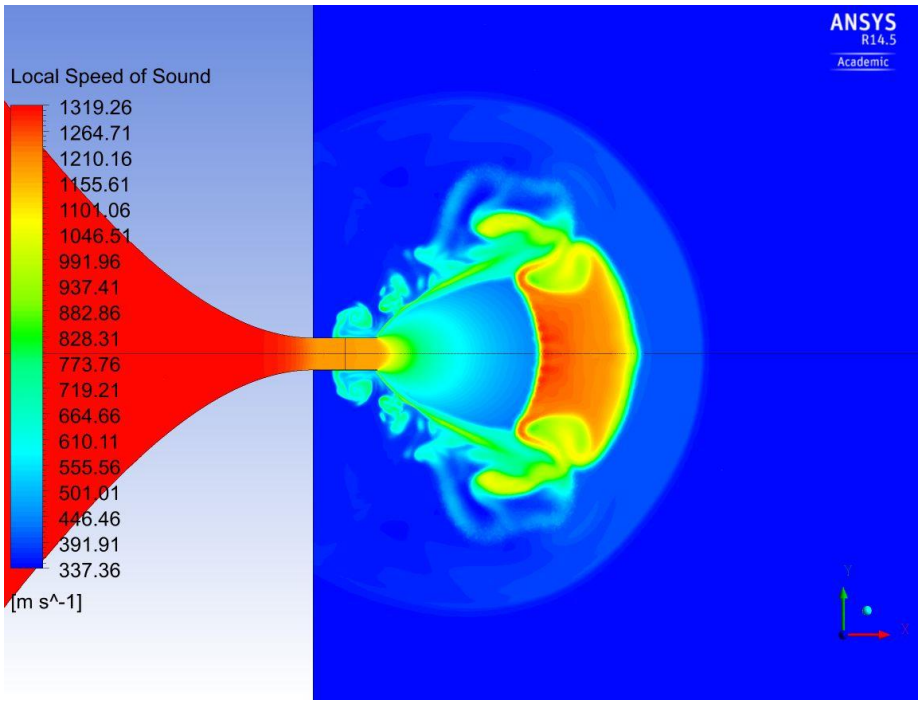

Figure 5-4: Local speed of sound contour at 15 µs time after the release

Sound travels slower in the gases, faster in liquids and much faster in solids. Sound travels at 343.2 m/s in air, it travels at 1484 m/s in water and 5120 m/s in iron. It is worth mentioning that in the exceptionally stiff material like diamond, sound travels at 12,000 m/s which is around the maximum speed that sound can travel in normal conditions.

Figure 5-5 shows the flow local speed of sound distribution along the centerline at t=15µs after the release. In the highly-pressurized hydrogen storage tank, the local speed of sound is high and is equal to 1319.26 m/s. It decreases toward the pipe exit and this decreasing trend continues up to the Mach disk. The flow local speed of sound experiences a big jump by passing through the Mach disk.

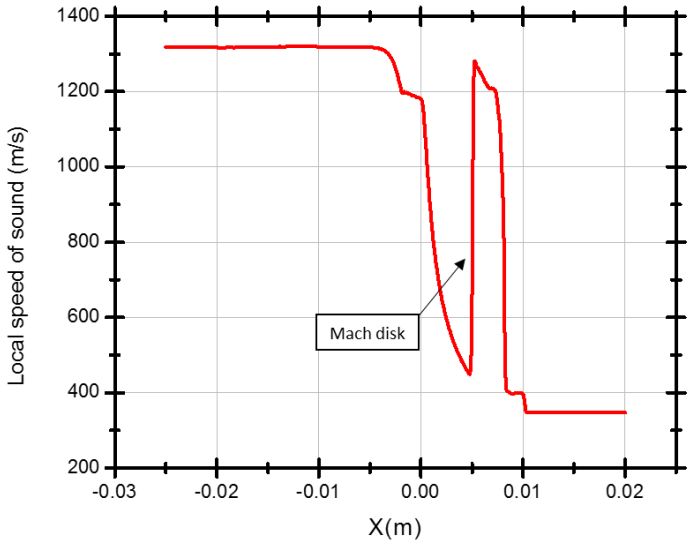

Figure 5-5: Local speed of sound distribution along the centerline at 15 μs after the release

5.1.2 Converging Diverging Boundary Layer Phenomena

According to the one-dimensional theory for constant area pipe flows, the flow accelerates along the pipe toward the pipe exit. The flow velocity can increase up to the speed of sound but can't exceed this speed. The flow at the nozzle exit become sonic and the Mach number is equal to unity. This is known as the choked phenomena.

Figure 5-6 shows the flow Mach number distribution along the pipe centerline for the case with initial tank pressure and temperature of $P_0 = 10$ MPa and $T_0 = 300$ K at t=50μs after release. Viscous terms and boundary layer effects are taken into consideration in the current CFD analysis. On the horizontal axis, $\frac{X}{L} = 0$ signifies starting point of the straight pipe and $\frac{X}{L} = 1$ signifies the pipe exit. It is seen that the actual throat section where the flow reaches sonic condition and the flow Mach number is equal to unity occurs not at the pipe exit, but upstream. This is in conflict with one dimensional theory for constant area pipe flows. Downstream of the actual throat section, flow accelerates to a speed higher than speed of sound and the flow is supersonic.

This is expected to be due to the boundary layer effect. Boundary layer thickness increases along the pipe toward the pipe exit. In the region near the pipe exit, a sudden decrease in the boundary layer thickness is seen. This generates a fictitious converging diverging nozzle. The actual throat where the flow reaches the sonic condition is the throat of this fictitious converging diverging nozzle and won't be at the pipe exit.

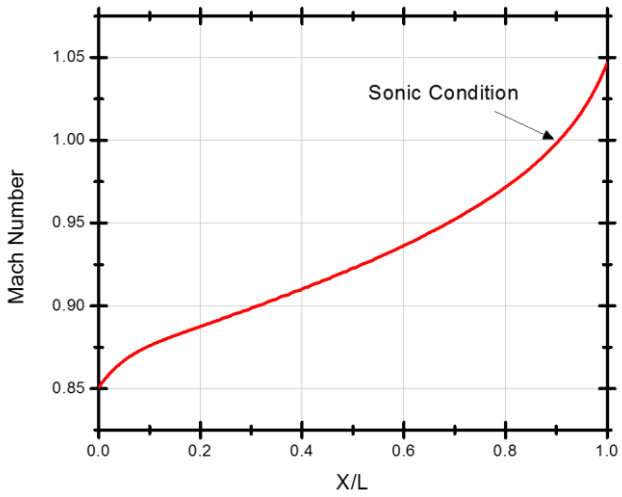

Figure 5-6: Th flo Mach number distribution along the pipe centerline

To provide better visualization of the converging diverging phenomena of the boundary layer, the flow Mach number distribution contours inside the pipe are shown in Figure 5-7 . The boundary layer thickness increases along the pipe wall up to a point close to the pipe exit. Then, it starts to decrease toward the pipe exit. The sonic condition doesn't occur at the pipe exit; it takes place at the throat section of the fictitious converging diverging nozzle formed by boundary layer.

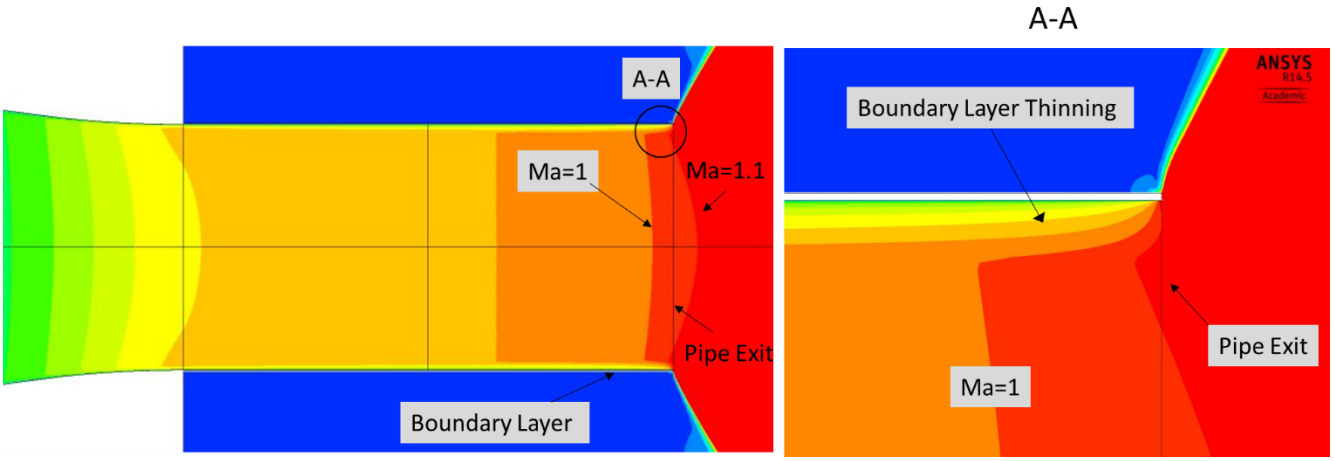

Figure 5-7: Th flo Mach number distribution inside the straight pipe

Figure 5-8 shows the schematic diagram of the flow inside the constant area pipe. Comparison is made between the inviscid one-dimensional theory (Figure 5-8-a) and the actual flow with consideration of viscous terms and boundary layer effects (Figure 5-8-b). For the inviscid one dimensional theory, the flow Mach number is equal to unity at the pipe exit and the flow sonic condition occurs at this location. No boundary layer is formed on the pipe walls and the flow velocity is uniformly distributed in the radial direction.

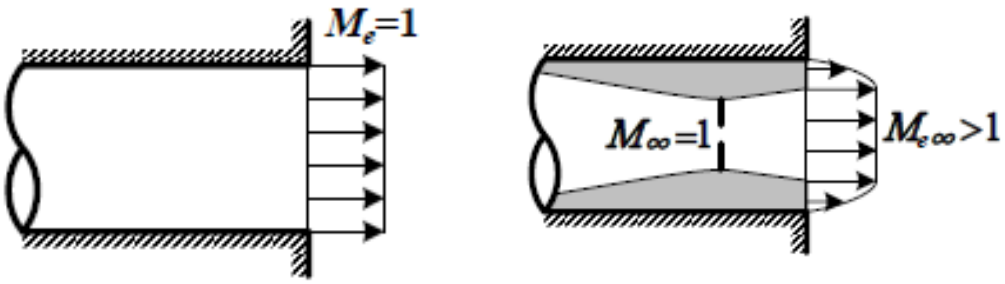

(a) one dimensional inviscid theory *(b) viscous flow*

Figure 5-8: Schematic diagram of the flo inside the constant area pipe [21]

(Figure 5-8-b) shows the formation of the boundary layer for the case considering fluid viscosity. The boundary layer thickness increases along the pipe toward the pipe exit. In the region near the pipe exit, it starts to decrease. This forms a fictitious converging diverging nozzle.

The flow velocity distribution in the radial direction at two different sections inside the straight pipe is illustrated in Figure 5-9. Due to the no-slip wall boundary condition which is applied to the straight pipe walls, the tangential velocity of the flow at the pipe wall is zero and the fluid flow comes to a complete stop.

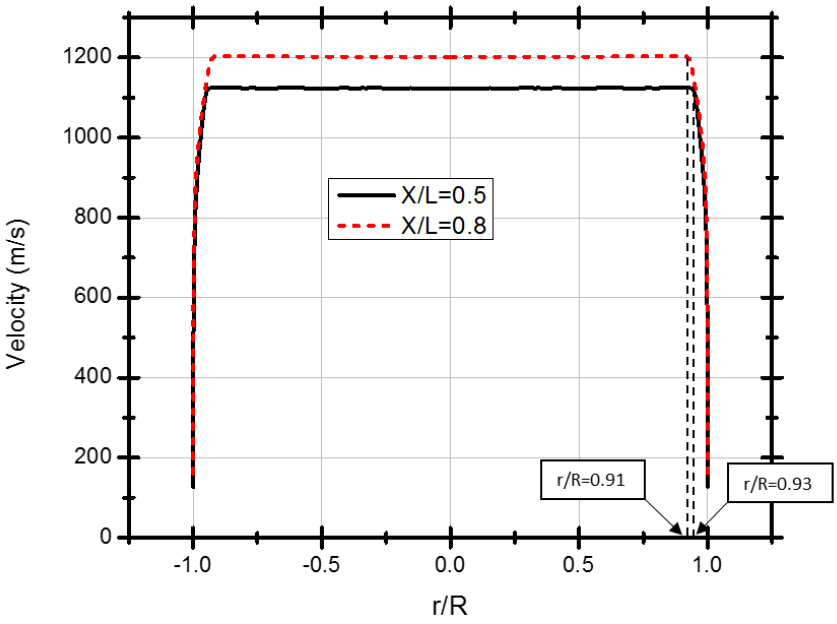

Figure 5-9: Th flo velocity distribution in radial direction inside the pipe at two different locations at t=50μs

The main flow free stream velocity is higher at the section closer to the pipe exit which indicates acceleration of the flow along the pipe. The boundary layer is thicker for the section closer to the pipe exit. The boundary layer thickness is δ=0.07 R (7% of the pipe radius) and δ=0.09 R (9% of the pipe radius) at $\frac{X}{L} = 0.5$ and $\frac{X}{L} = 0.8$, respectively. The boundary layer thickness grows along the flow direction up to a certain point, near the pipe exit. Downstream of this section, the boundary layer thickness starts to decrease which forms a fictitious converging diverging nozzle.

5.1.3 Comparison of Viscous and Inviscid Simulations

In this section, the viscous and inviscid simulations are compared to investigate how the flow viscosity and the boundary layer formation affect the properties inside the pipe. Figure 5-10 shows the flow properties for the case with initial tank pressure and temperature of $P_0 = 10$ MPa and $T_0 = 300$ K . In the inviscid simulations, the viscosity is not considered and slip wall boundary condition is applied to the pipe walls. Without formation of the boundary layer, the flow is characterized as a bulk motion and the flow properties are uniformly distributed along the radial direction.

According to Figure 5-10 , Inviscid simulations lead to lower density, temperature and pressure at the pipe exit, while higher velocity is obtained.

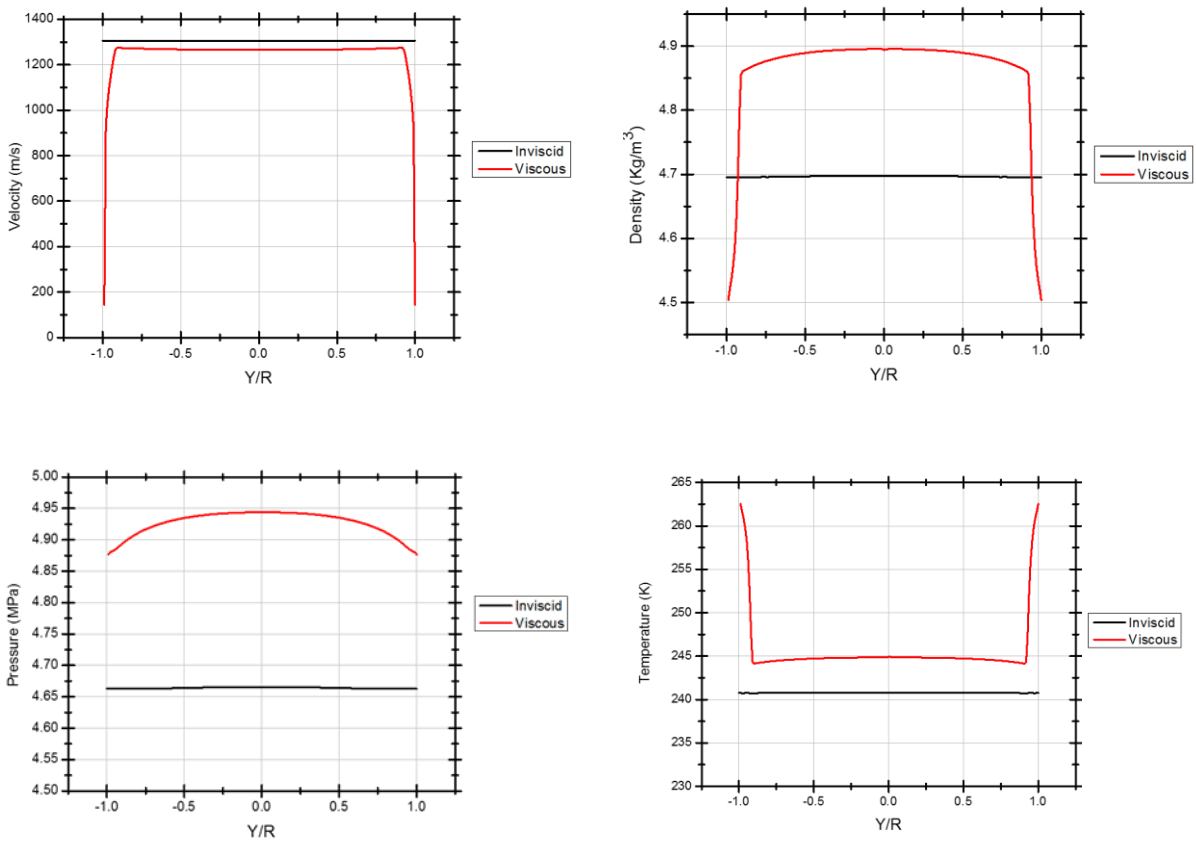

Figure 5-10 : The flo properties radial distribution at the pipe exit; comparison of viscous and inviscid simulations

The mass concentration contour for the viscous and inviscid simulations at t=30µs after release is presented in Figure 5-11. Reviewing the contours shows that the flow has very similar behaviour for these two simulations.

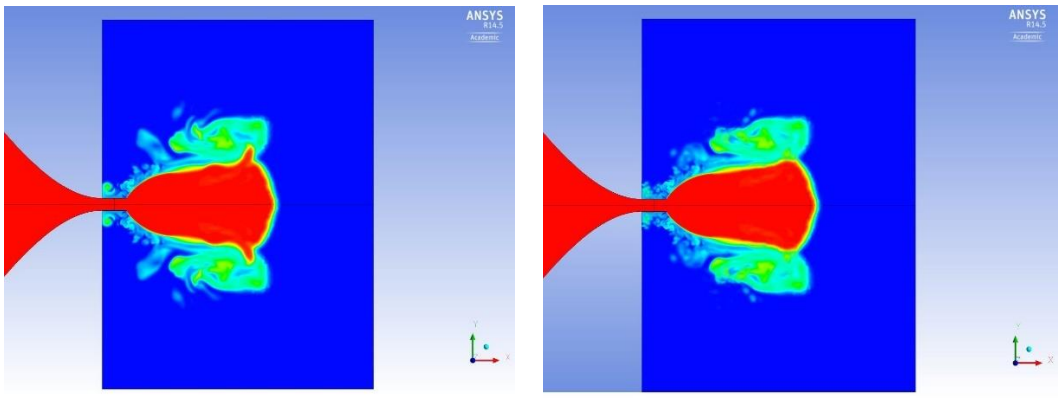

Figure 5-11 : Mass concertation contour at t=30µs after release: Viscous (Left) and Inviscid simulation (Right)

5.2 The Flow Evolution

5.2.1 Time Evolution of the Flow Properties inside The Pipe

Figure 5-12 shows the flow Mach number distribution along the pipe centerline for the case with initial tank pressure and temperature of P_0=10 MPa and $T_0 = 300$ K at diff rent times of release. The flow accelerates along the pipe and the Mach number increases toward the pipe exit. Th fl w properties are time dependent. Higher Mach number values are seen for the early times of release and it decreases with time. The rate of change is high at early stages and gets lower over time. After some point, during the release, instantaneous changes disappear and the flow characteristic reaches the choked flow conditions.

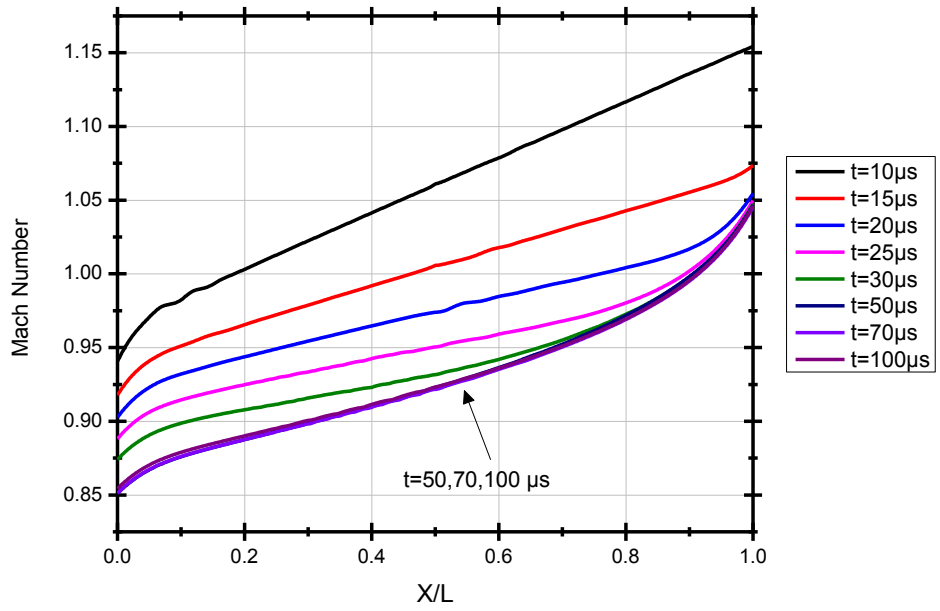

Figure 5-12: Mach number distribution along the pipe centerline at different times of release

The flow properties as well as the sonic line position and the Mach number at the pipe exit experience big changes in early stages of the release and gradually get to a state with negligible changes. The flow Mach number at the pipe exit decreases over time. It should be mentioned that

for all times, the Mach number at the pipe exit is above unity and the flow has supersonic conditions.

Figure 5-13 and Figure 5-14 show density and pressure distributions along the pipe centerline at diff rent times of the release, respectively. The flow properties are time dependent and vary with time.

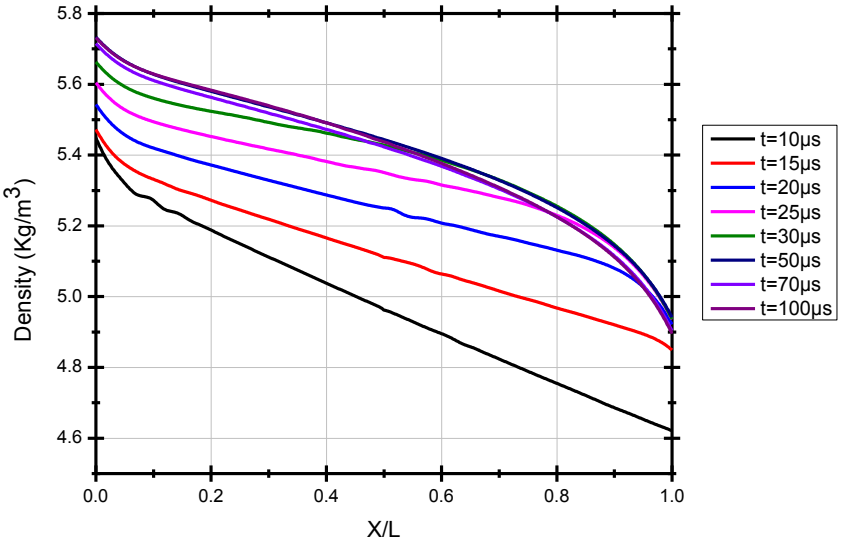

Figure 5-13: Density distribution along the pipe centerline at different times of the release

The flow density has a decreasing trend along the pipe, toward the pipe exit. The density increases over time; lower values of density are seen for early stages of release and higher values for later stages.

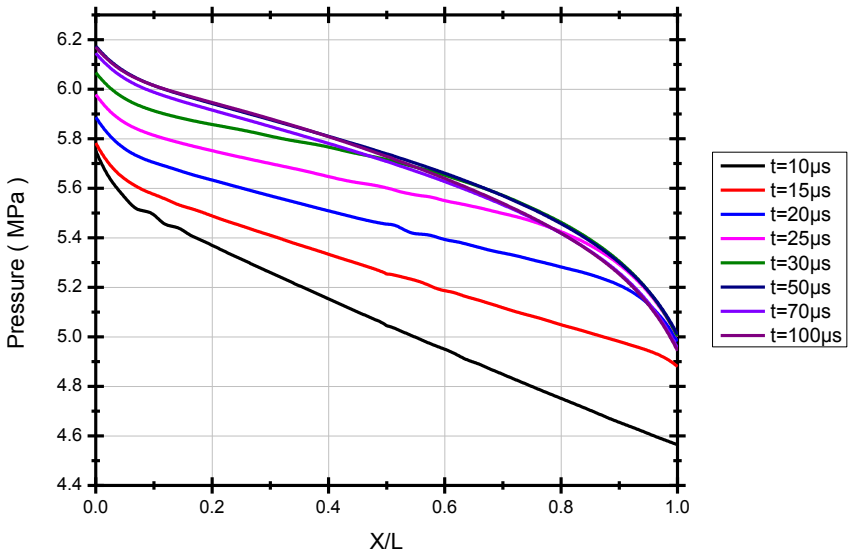

Figure 5-14: Pressure distribution along the pipe centerline at different times of the release

The flow pressure has a decreasing trend along the pipe, toward the pipe exit. The pressure increases over time; lower values of pressure are seen for the early stages of the release. At some point during the release, the rate of change becomes slower and the flow properties get into a state with negligible changes. It should be mentioned that, for all the simulation times the flow pressure at the pipe exit, leaving the hydrogen storage tank, is higher than the ambient pressure and the jet flow is highly under expanded. The flow expansion is not complete inside the pipe and further expansion occurs downstream of the pipe exit.

The flow evolution is further discussed in APPENDIX B and APPENDIX C. The flow properties contour at diff rent times of release are presented in APPENDIX B. The distribution of the flow properties along the centerline is provided in APPENDIX C.

5.2.2 The Flow Properties Radial Distribution at the Pipe Exit

Figure 5-15 and Figure 5-16 show the flow properties distribution in the radial direction at the pipe exit for the case with initial tank pressure of $P_0 = 10$ MPa. The flow properties are reported at diff rent times of the release to investigate the flow evolution. In the current CFD study, the flow viscosity and the boundary layer effects are taken into consideration.

Figure 5-15 shows the Mach number radial distribution at the pipe exit section. As illustrated, in all times of the release, the Mach number is higher than unity and the flow has supersonic conditions at the exit section. Due to the flow viscosity and no slip boundary condition which is applied to the pipe walls the flow velocity is zero adjacent to the wall.

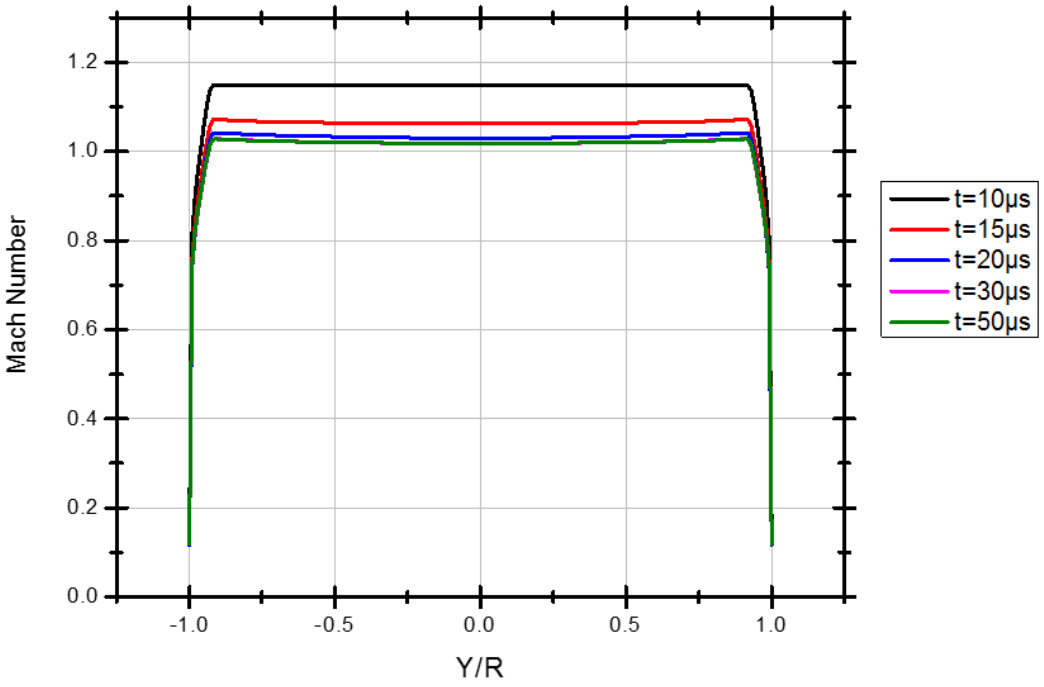

Figure 5-15: Mach number radial distribution at the pipe exit at different times of the release

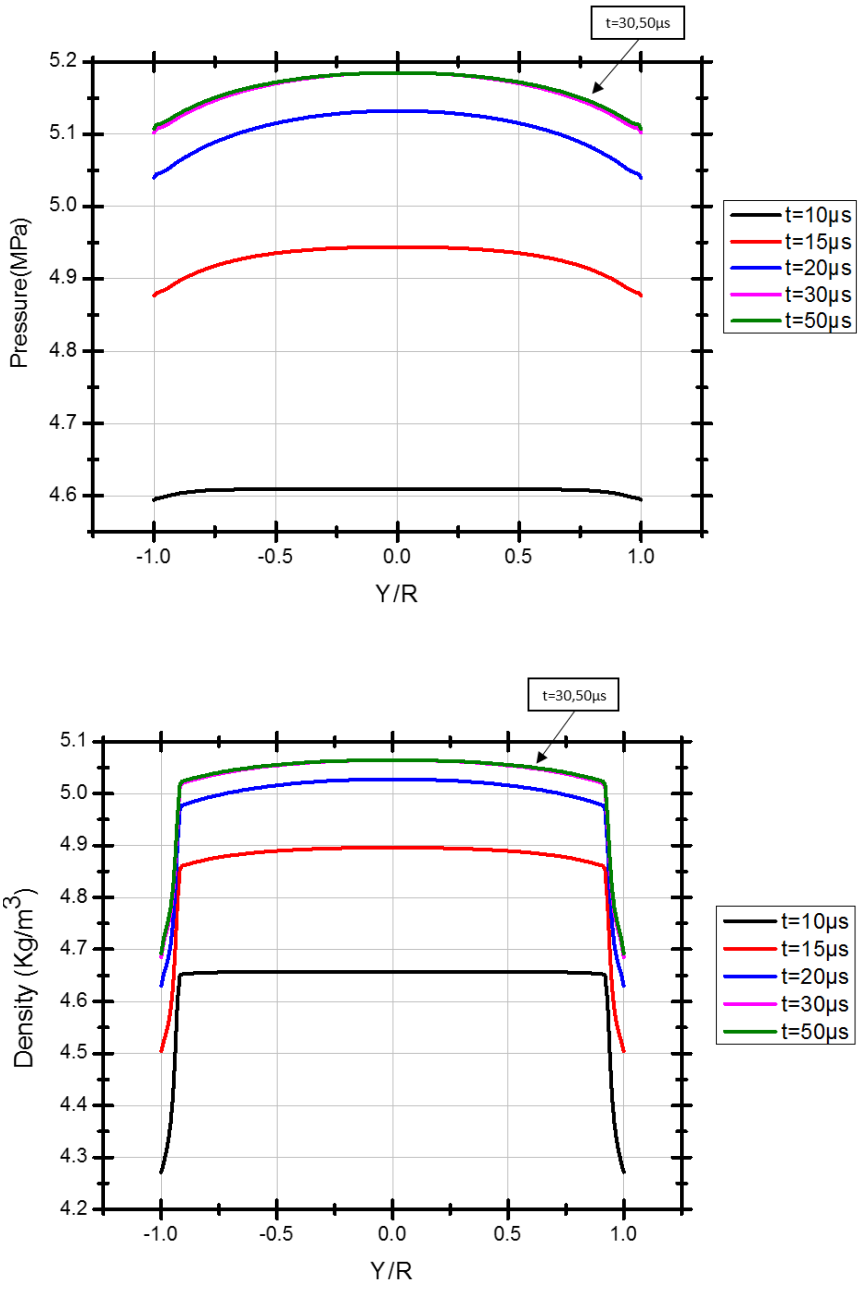

Figure 5-16 : Flow properties radial distribution at the pipe exit at different times of the release

Figure 5-16 shows the pressure and density radial distributions. During the hydrogen release from the storage tank, the pressure at the exit section increase with time.

During the release, the flow density at the pipe exit section increases with time. The rate of change in the early stages of release is high and as time passes, the changes in the flow properties become slower.

5.3 Different Tank Initial Pressure Investigation

Hydrogen has low energy density per volume. This hydrogen property urges us to use highly pressurized storage tanks to store energy. Hydrogen release from two tanks with different initial tank pressures of $P_0 = 10$ MPa and $P_0 = 70$ MPa ,which have real life industrial applications, are explored. Figure 5-17 and Figure 5-18 show the flow Mach number and velocity distribution along the pipe centerline at t=50μs of the release, respectively.

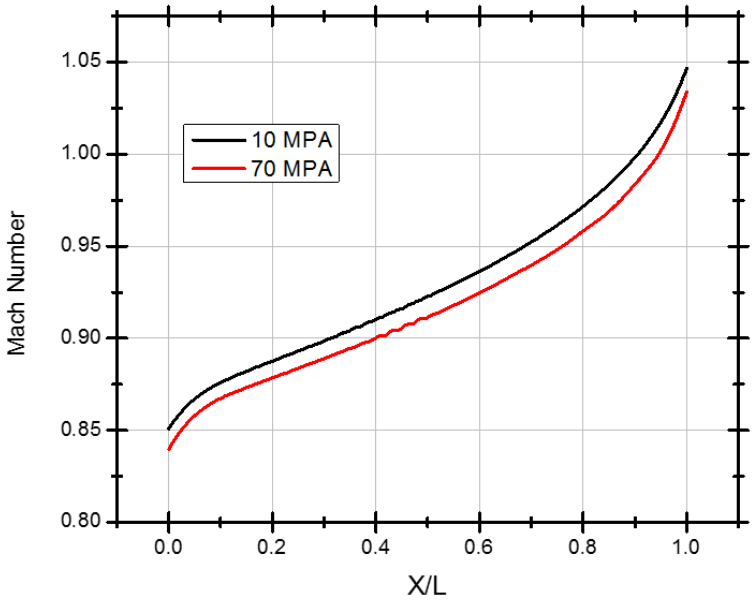

Figure 5-17: Mach number distribution along the pipe centerline for different initial tank pressure:

The flow Mach number is increasing towards the pipe exit and the sonic condition takes place upstream of the exit section. The flow reaches the sonic condition at the actual throat of the fictitious converging diverging nozzle formed by the boundary layer. The flow is supersonic at the exit section of the pipe.

The higher tank pressure leads to a smaller boundary layer thickness and therefore to a smaller supersonic flow at the pipe exit. The flow Mach number at the pipe exit is closer to unity for the higher-pressure storage tank.

The flow velocity and the local speed of sound along the pipe centerline are presented in Figure 5-18 and Figure 5-19. A higher tank pressure leads to higher flow velocities and higher local speed of sound inside the pipe.

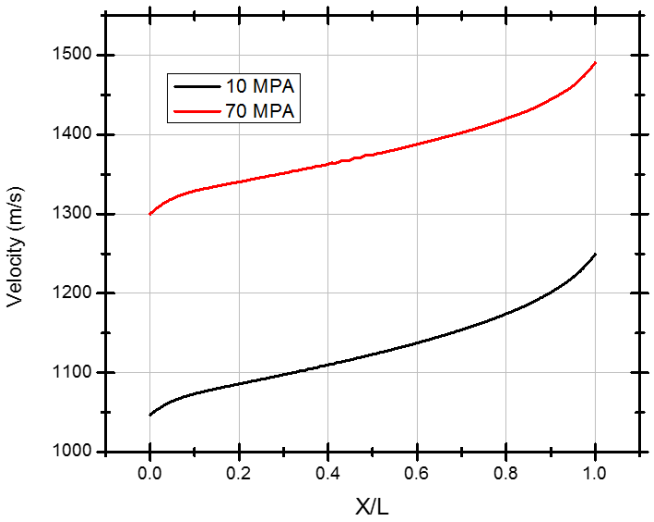

Figure 5-18: Flow Velocity along the pipe centerline for different initial tank pressure

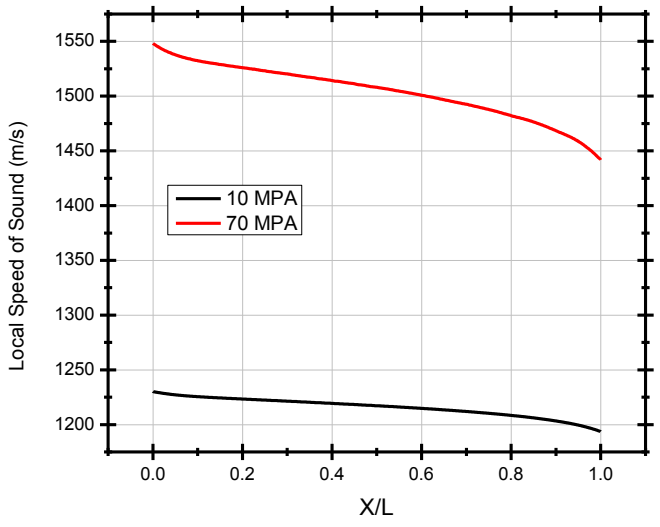

Figure 5-19: Local speed of sound along the pipe centerline for different initial tank pressure

5.4 Different Tank Initial Temperature Investigation

In this section, the hydrogen release from two tanks with diff rent initial temperatures of $T_0 = 300$ K and $T_0 = 200$ K are explored at t=30μs after the release. Figure 5-20 shows the flow Mach number distribution along the pipe centerline. Higher Mach number is seen in the pipe for the lower temperature up to a point near the pipe exit. In the region near the pipe exit, the Mach number for both cases is the same.

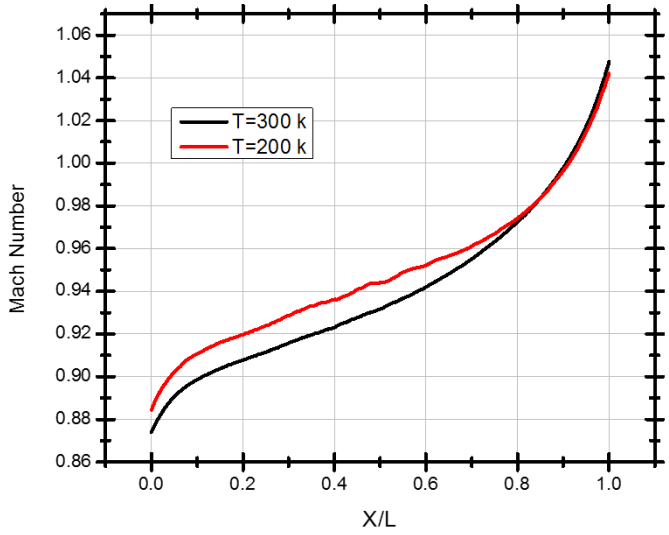

Figure 5-20 : Mach number distribution along the pipe centerline for different initial tank temperatures

Figure 5-21 shows the velocity and the local speed of sound distribution along the pipe centerline. Higher flow velocities and higher local speed of sound are observed for the tank with lower initial temperature.

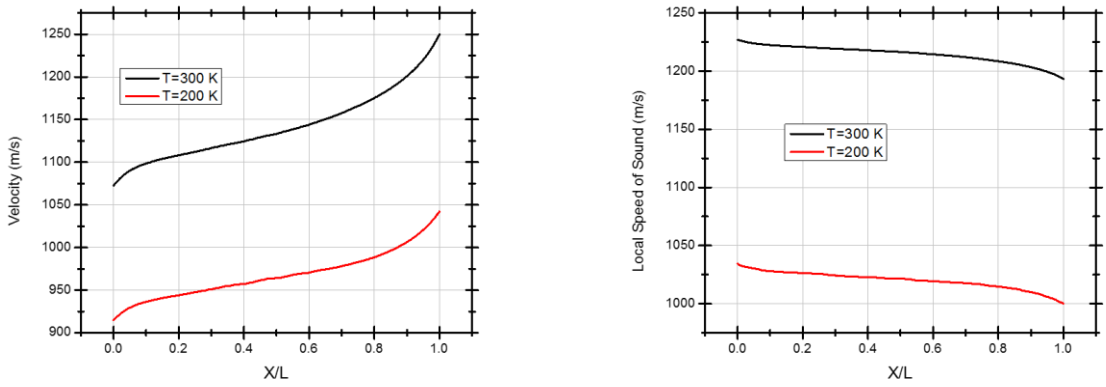

Figure 5-21 : The flo properties distribution along the pipe centerline for different initial tank temperatures: The flo velocity (left) and the flo local speed of sound (right)

Figure 5-22 shows the pressure and the density distribution along the pipe centerline. The cryogenic hydrogen storage (Tank with $T_0 = 200K$) has higher density and lower pressure inside the release pipe.

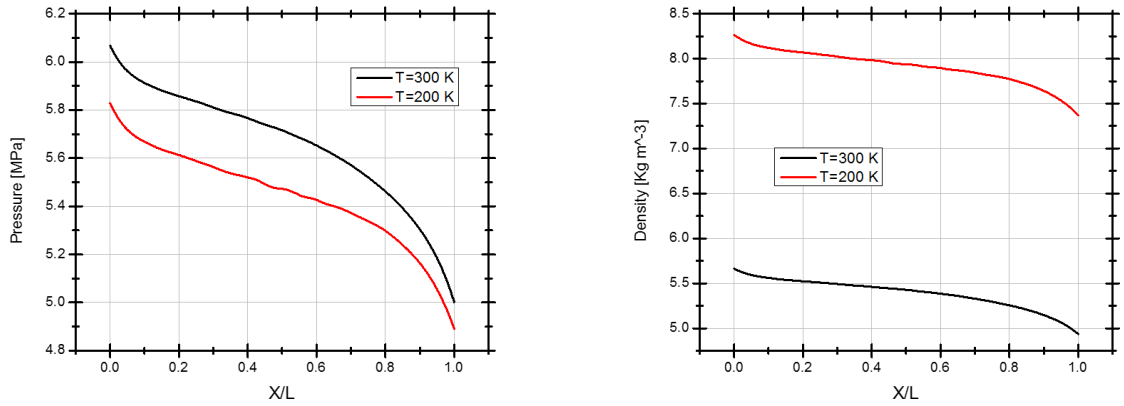

Figure 5-22: The flo properties distribution along the pipe centerline for different initial tank temperatures: The flo pressure (left) and the fl w density (right)

5.5 Hydrogen Mass Flow Rate

In this section, the hydrogen mass flow rate exiting the high-pressure storage tank is explored. Two diff rent storage tanks with initial tank pressures of $P_0 = 10$ MPa and $P_0 = 70$ MPa are investigated and the results are provided in *Table 5-1*.

The high-pressure ratio between the reservoir and the atmosphere leads to highly under-expanded jet flow. The flow is choked and the mass flow rate becomes constant.

The mass flow rate is slightly overestimated with inviscid simulations. Comparing the viscous and inviscid simulations with and initial pressure of $P = 10$ MPa shows 1.65% lower mass flow rate for the viscous case.

As mentioned earlier, the higher tank pressure leads to a smaller boundary layer thickness. Comparing the viscous and inviscid simulations for $P = 70$ MPa shows a diff rence of less than 1% in the mass flow rate. This investigation shows smaller effects of fluid viscosity in the higher tank pressures.

Higher mass flow rate is obtained for a higher tank pressure. The mass flow rate from a tank with $P = 70$ MPa is 6.53 times the rate for $P = 10$ MPa.

	$P_0 = 10$ MPa $T_0 = 300$ K		$P_0 = 70$ MPa $T_0 = 300$ K		$P_0 = 10$ MPa $T_0 = 200$ K
	Viscous	Inviscid	Viscous	Inviscid	Viscous
Mass flow rate (kg/s)	0.00474	0.00482	0.03098	0.03119	0.00592

Table 5-1: Hydrogen mass flo rate exiting the high-pressure storage tank

The cryogenic storage of hydrogen leads to higher density in the tank and ultimately gives a higher mass flow rate. Lowering the initial tank temperature from $T = 300$ K to $T = 200$ K results in a 24.89% increase in the mass flow rate.

CHAPTER 6

CONCLUSIONS AND FUTURE WORK

6.1 Conclusions

Hydrogen has small energy per volume which requires high pressure gaseous storage systems. In the current study, sudden release of the hydrogen from a high-pressure storage tank is investigated to further understand the flow behavior at the exit and near the exit region.

The numerical simulation is conducted using the Ansys CFX commercial software. Unsteady compressible Navier-Stokes equations with an additional transport equation are the governing equations of the fluid flow. The second order backward Euler method is implemented for the time discretization. The high-resolution scheme is applied for the convective term which makes the CFD simulations second order in space. The two-equation shear stress transport (SST) $k - \omega$ turbulence model is used to investigate the turbulent features of the flow.

Thermodynamic behavior of hydrogen at high pressures deviates from predicted properties of the ideal gas law. Accurate predictions of the hydrogen properties at high pressure require a real gas equation of state. In the numerical analysis, the Peng-Robinson EOS is used as a real gas model.

The flow release properties, calculated by an analytical model, are used to validate the CFD analysis. The comparison between these two models shows good agreement. In addition to the analytical model, the accuracy of the CFD analysis is also verified with a previous work in the literature done by Afroosheh et al. [25].

The under expanded jet flow is complex and a number of shocks and discontinuities with high gradients in the flow properties occur in the flow. This complex flow requires a very stable code with high quality mesh to capture all the flow features. The flow structure, predicted by the CFD analysis is compared with the expected flow structure of the highly under expanded jet flows

provided by Grist et al. [30] and the comparison shows that the results are in good agreement and all the flow features are well captured in the current analysis.

The simulation of viscous flow shows that the flow has supersonic condition at the pipe exit. Unlike the one-dimensional theories for the constant pipe flows, the flow Mach number is beyond unity at the pipe exit. This is due to the boundary layer formation on the pipe walls. The boundary layer thickness increases along the pipe toward the pipe exit. In the region near the pipe exit, a sudden decrease in the boundary layer thickness is seen. This generates a fictitious converging diverging nozzle. The actual throat where the flow reaches the sonic condition is the throat of this fictitious converging diverging nozzle.

Hydrogen release from two storage tanks with diff rent initial tank pressures of $P_0 = 10MPa \; and \; P_0 = 70MPa$ are explored. The higher tank pressure leads to a smaller boundary layer thickness and therefore to a smaller supersonic flow at the pipe exit.

The hydrogen release from storage tanks with diff rent initial tank temperatures of $T_0 = 300 \; K \; and \; T_0 = 200 \; K$ are explored. The velocities and the local speed of sound are lower for the lower tank temperature. Furthermore, The Mach number in the release pipe shows similar behavior near the exit region.

The hydrogen mass flow rate exiting the high-pressure storage tank is investigated and it is concluded that inviscid simulations slightly overestimate the hydrogen flow rate. Considering the flow viscosity and viscous terms for the case with initial tank pressure of $P = 10MPa$ result in 1.65% lower mass flow rate. This diff rence is less than 1% for the $P_0 = 70MPa$, which indicates smaller boundary layer formation and smaller fluid viscosity effects for higher tank pressures.

6.2 Future Work

This work has investigated hydrogen release from a high-pressure storage tank with consideration of flow viscosity, in details. The boundary layer effects on the mass flow rate is small but it leads to Mach number beyond unity at the exit region. A spontaneous ignition can occur in the high-pressure hydrogen jet. To simulate this phenomenon, the simulation needs to be extended. The following future tasks are proposed:

- The chemical reaction between the species in the hydrogen-air mixture can be investigated;
- The model can be expanded to study the spontaneous ignition and combustion of the hydrogen jet.

REFERENCES

[1] M. Brower *et al.*, "Renewable Enery - Global Status Report (GSR 2014)," 2014.

[2] B. V. Mathiesen *et al.*, "Smart Energy Systems for Coherent 100% Renewable Energy and Transport Solutions," *Appl. Energy*, vol. 145, pp. 139–154, 2015.

[3] "Energy Resources Department of Goverment of Canada." [Online]. Available: http://www.nrcan.gc.ca/energy.

[4] "US Energy Department." [Online]. Available: www.hydrogen.energy.gov.

[5] "BMW Hydrogen Vehicle Data Sheet." [Online]. Available: www.bmw.com.

[6] "Wikipedia." [Online]. Available: www.wikipedia.org.

[7] J. Zheng, X. Liu, P. Xu, P. Liu, Y. Zhao, and J. Yang, "Development of High Pressure Gaseous Hydrogen Storage Technologies," *Int. J. Hydrogen Energy*, vol. 37, no. 1, pp. 1048–1057, 2012.

[8] M. Wietschel and M. Ball, *Th Hydrogen Economy*. 2006.

[9] F. Zhang, P. Zhao, M. Niu, and J. Maddy, "The Survey of Key Technologies in Hydrogen Energy Storage," *Int. J. Hydrogen Energy*, vol. 41, no. 33, pp. 14535–14552, 2016.

[10] J. Wallace, "a Comparison of Compressed Hydrogen and CNG Storage," *Int. J. Hydrogen Energy*, vol. 9, no. 7, pp. 609–611, 1984.

[11] L. A. McCarty, Robert D.; Weber, *Thermophysical Properties of Parahydrogen from the Freezing Liquid Line to 5000 R for Pressures to 10,000 Psia*. 1972.

[12] McCarty RD, *Hydrogen Technological Survey: Thermophysical Properties*. 1975.

[13] H. M. McCarty, R.D. ; Hord, J. ; Roder, *Selected Properties of Hydrogen (Engineering Design Data)*. 1981.

[14] R. C. Johnson, "Real Gas Effects in Flow Metering," pp. 1–169, 2010.

[15] R. C. Johnson, "Calculations of Real-Gas Effects in Flow Through Critical-Flow

Nozzles," 1965.

[16] K. Mohamed, "Simulation of Hydrogen Release from a High-Pressure Chamber Considering Real Gas Effects," Concordia University, 2004.

[17] R. Khaksarfard, M. R. Kameshki, and M. Paraschivoiu, "Numerical Simulation of High Pressure Release and Dispersion of Hydrogen into Air with Real Gas Model," *Shock Waves*, vol. 20, no. 3, pp. 205–216, 2010.

[18] K. Nasrifar, "Comparative Study of Eleven Equations of State in Predicting the Thermodynamic Properties of Hydrogen," *Int. J. Hydrogen Energy*, vol. 35, no. 8, pp. 3802–3811, Apr. 2010.

[19] F. Markert, D. Melideo, and D. Baraldi, "Numerical Analysis of Accidental Hydrogen Releases from High Pressure Storage at Low Temperatures," *Int. J. Hydrogen Energy*, vol. 39, no. 14, pp. 7356–7364, 2014.

[20] J. Nagao, S. Matsuo, S. Suetsugu, T. Setoguchi, and H. D. Kim, "Characteristics of High Reynolds Number Flow in a Critical Nozzle," *Int. J. Hydrogen Energy*, vol. 38, no. 21, pp. 9043–9051, 2013.

[21] K. Kubo, Y. Miyazato, and K. Matsuo, "Study of Choked Flows Th ough a Convergent Nozzle," *Int. J. Th rm. Sci.*, vol. 19, no. 3, pp. 193–197, 2010.

[22] T. Yoshimaru, Y. Asako, and T. Yamada, "Under-expanded Gaseous Flow at a Straight Micro-Tube Exit," *J. Fluids Eng.*, vol. 136, no. c, pp. 1–7, 2014.

[23] V. Lijo, H. D. Kim, and T. Setoguchi, "Analysis of Choked Viscous Flows through a Constant Area Duct," *J. Aerosp. Eng.*, vol. 224, no. 11, pp. 1151–1162, 2010.

[24] A. Hamzehloo and P. G. Aleiferis, "Large Eddy simulation of Highly Turbulent Under-Expanded Hydrogen and Methane Jets for Gaseous-Fuelled Internal Combustion Engines," *Int. J. Hydrogen Energy*, vol. 39, no. 36, pp. 21275–21296, 2014.

[25] M. Afroosheh, "Large Eddy Simulation of Hydrogen Sonic Jet," Concordia University, 2014.

[26] B. Chernyavsky, T. C. Wu, F. Péneau, P. Bénard, P. Oshkai, and N. Djilali, "Numerical

and Experimental Investigation of Buoyant Gas Release: Application to Hydrogen Jets," *Int. J. Hydrogen Energy*, vol. 36, pp. 2645–2655, 2011.

[27] F. Ganci, A. Carpignano, N. Mattei, and M. N. Carcassi, "Hydrogen Release and Atmospheric Dispersion: Experimental Studies and Comparison with Parametric Simulations," *Int. J. Hydrogen Energy*, vol. 36, no. 3, pp. 2445–2454, 2011.

[28] A. G. Venetsanos and S. G. Giannissi, "Release and Dispersion Modeling of Cryogenic Under-Expanded Hydrogen Jets," *Int. J. Hydrogen Energy*, 2016.

[29] T. Adamson and J. Nicollas, "On the Structure of Jets from Highly Under-Expanded Nozzles into Still Air," *J. Aerosp. Sci.*, vol. 26, no. 1, pp. 16–24, 1959.

[30] S. Grist and P. M. Sherman, "Study of the Highly UnderExpanded Sonic Jets," *AIAA J.*, vol. 4, no. 1.

[31] J. a. Wilkes, C. E. Glass, P. M. Danehy, and R. J. Nowak, "Fluorescence Imaging of Underexpanded Jets and Comparison with CFD," *Am. Inst. Aeronaut. Astronaut.*, no. January, 2006.

[32] E. G. Merilo, M. A. Groethe, J. D. Colton, and S. Chiba, "Experimental Study of Hydrogen Release Accidents in a Vehicle Garage," *Int. J. Hydrogen Energy*, vol. 36, no. 3, pp. 2436–2444, 2011.

[33] S. H. Han and D. Chang, "Numerical and Experimental Study of Hydrogen Release from a High-Pressure Vessel," *Adv. Intell. Soft Comput.*, vol. 145 AISC, no. VOL. 2, pp. 489–494, 2012.

[34] W. Breitung, G. Necker, B. Kaup, and A. Veser, "Numerical Simulation of Hydrogen Release in a Private Garage," *Proc. Hypothesis IV*, no. September, pp. 9–14, 2001.

[35] J. S. Mukai, H. Mitsuishi, and K. O. S. Watanabe, "CFD Simulation of Hydrogen Leakage Caused by Fuel Cell Vehicle Accident in Tunnel, Underground Parking Lot and Multistory Parking Garage," *Japan Automob. Res. Institue*, vol. 27, 2005.

[36] M. V. Bragin and V. V. Molkov, "Physics of Spontaneous Ignition of High-Pressure Hydrogen Release and Transition to Jet Fire," *Int. J. Hydrogen Energy*, vol. 36, no. 3, pp.

2589–2596, 2011.

[37] B. P. Xu, L. El Hima, J. X. Wen, S. Dembele, V. H. Y. Tam, and T. Donchev, “Numerical Study on the Spontaneous Ignition of Pressurized Hydrogen Release through a Tube into Air,” *J. Loss Prev. Process Ind.*, vol. 21, no. 2, pp. 205–213, 2008.

[38] P. P. Panda and E. S. Hecht, “Ignition and Flame Characteristics of Cryogenic Hydrogen Releases,” *Int. J. Hydrogen Energy*, 2016.

[39] F. Dryer, M. Chaos, Z. Zhao, J. N. Stein, J. Alpert, and C. J. Homer, “Spontaneous Ignition of Pressurized Releases of Hydrogen and Natural Gas Into Air,” *Combust. Sci. Technol.*, vol. 179, no. 4, pp. 663–694, 2007.

[40] T. Mogi, D. Kim, H. Shiina, and S. Horiguchi, “Self-Ignition and Explosion during Discharge of High-Pressure Hydrogen,” *J. Loss Prev. Process Ind.*, vol. 21, no. 2, pp. 199–204, 2008.

[41] V. Golub *et al.*, “Mechanisms of High-Pressure Hydrogen Gas Self-Ignition in Tubes,” *J. Loss Prev. Process Ind.*, vol. 21, no. 2, pp. 185–198, 2008.

[42] J. X. Wen, B. P. Xu, and V. H. Y. Tam, “Numerical Study on Spontaneous Ignition of Pressurized Hydrogen Release through a Length of Tube,” *Combust. Flame*, vol. 156, no. 11, pp. 2173–2189, 2009.

[43] *ANSYS CFX-Solver Th ory Guide*, no. April. 2009.

[44] F. R. Menter, “Two-Equation Eddy-Viscosity Turbulence Models for Engineering Applications,” *AIAA J.*, vol. 32, no. 8, pp. 1598–1605, 1994.

[45] G. J. Van Wylen, *Fundamentals of Th rmodynamics*. .

[46] “NIST-JANNAF Thermochemical Tables,” *J. Phys. Chem. Ref. Data*, 1998.

APPENDIX A

ANALYTICAL MODEL DEVELOPMENT

A.1 Conservation Equations

In this section, the assumptions which were mentioned in the section 2.5 are used to write the conservation equations and to derive thermodynamics relations. This model is developed by Mohamed et al. [16] . The conservation of mass and energy equations inside the control volume (depicted in *Figure 2-2*) are as follows:

- Conservation of mass:

$$\frac{\partial}{\partial t}\left(\frac{\Psi}{v_t}\right) = -\frac{a_n A_n}{v_n} \qquad \text{(A-1)}$$

- Conservation of energy:

$$\frac{\partial}{\partial t}\left(\frac{\Psi i_t}{v_t}\right) = -\frac{(h_{\mathrm{n}} + 0.5{a_n}^2)\, a_n\, A_n}{v_n} \qquad \text{(A-2)}$$

Expanding the derivatives on the left-hand side of the equations *(A-1)* and *(A-2)* , the equations can be rewritten as:

$$-\frac{\Psi}{{v_t}^2}\frac{\partial v_t}{\partial t} = -\frac{a_n A_n}{v_n} \qquad \text{(A-3)}$$

$$\frac{\Psi}{v_t}\frac{\partial i_t}{\partial t} - \frac{\Psi i_t}{{v_t}^2}\frac{\partial v_t}{\partial t} = -\frac{(h_n + 0.5{a_n}^2)\, a_n\, A_n}{v_n} \qquad \text{(A-4)}$$

After substituting $\frac{\partial v_t}{\partial t}$ from equation (A-3) into equation (A-4) and rearranging the above equations, final forms of conservation equations are obtained as:

$$\frac{\partial\, v_t}{\partial t} = \frac{{v_t}^2}{\Psi}\frac{a_n A_n}{v_n} \qquad \text{(A-5)}$$

$$\frac{\partial\, i_t}{\partial t} = -\frac{(h_n + 0.5{a_n}^2)\, a_n\, A_n}{\Psi}\frac{v_t}{v_n} + \frac{i_t\, a_n A_n}{\Psi}\,\frac{v_t}{v_n} \qquad \text{(A-6)}$$

Thermodynamic properties of the flow at the orifice appears only on the right-hand side of the conservation equations. In the following section, relations between dependent and independent flow properties are derived.

A.2 Thermodynamics Relations

Beattie-Bridgeman equation of state is taken as a real gas equation to develop the analytical model.

$$\mathrm{P} = f(T, v) = \frac{RT}{v} + \left(\frac{-cR}{T^2} + B_0 RT - A_0\right)\frac{1}{v^2} + \left(-\frac{B_0 cR}{T^2} - B_0 bRT + \alpha A_0\right)\frac{1}{v^3} + \frac{B_0 bcR}{T^2}\frac{1}{v^4} \qquad \text{(A-7)}$$

The flow pressure is explicitly given by two independent thermodynamic properties of temperature and specific volume. Table A-1 shows the constants of Beattie-Bridgeman equation of state for hydrogen.

A_0 $(m^5/Kg.s^2)$	$10^2 * B_0$ (m^3/Kg)	$10^3 * \alpha$ (m^3/Kg)	$10^2 * b$ (m^3/Kg)	$10^{-2} * c$ (m^3/Kg)
4924	1.034	-2.510	-2.162	2.5

Table A-1: Beattie-Bridgeman equation of state constants for hydrogen

Temperature and specific volume are selected as independent thermodynamic properties. Speed of sound, specific heats, internal energy and enthalpy are calculated in terms of temperature and specific volume. For a pure substance, the following thermodynamic relations exist between changes in entropy , temperature , pressure and specific volume [45] :

$$\mathrm{d}s = C_v \frac{dT}{T} + (\frac{\partial P}{\partial T})_v dv = C_P \frac{dT}{T} - (\frac{\partial v}{\partial T})_P dP \qquad \text{(A-8)}$$

In an isentropic process, entropy remains constant and equation *(A-8)* can be rewritten to the following forms:

$$(\frac{\partial T}{\partial v})_s = -\frac{T}{C_v}(\frac{\partial P}{\partial T})_v \qquad \text{(A-9)}$$

$$(\frac{\partial T}{\partial P})_s = \frac{T}{C_P}(\frac{\partial v}{\partial T})_P \qquad \text{(A-10)}$$

A.2.1 Specific Heats

Specific heats of hydrogen at constant pressure are tabulated in [46] for the range of temperature between $T = 0^0K \; to \; 6000^0K$ These values correspond to a reference pressure of $P = 0.1MPa$. At this reference pressure, hydrogen behaves like an ideal gas. These values should be modified for higher pressures because the behavior of the gas is deviating from the ideal gas predications.

To modify the specific heat and to calculate corresponding real values at a desired state the following procedure is taken:

The first step is to calculate the ideal value of specific heat,$\widetilde{C_P}$, at temperature T and for the reference pressure of $P = 0.1MPa$.This is done by searching through the hydrogen specific heats given in [46] .

The following ideal gas thermodynamic relations exist between the specific heat at constant volume and constant pressure:

$$\widetilde{C_v}(T) = \widetilde{C_P}(T) - R \qquad \text{(A-11)}$$

$$v^0 = \frac{RT}{10^5} \qquad \text{(A-12)}$$

In the second step, the value of specific heat which is given by equation *(A-11*) , is modified by assuming constant temperature process through which the specific volume of hydrogen is changed from v^0 to v.This process can be formulated as:

$$C_v(T,v) = \widetilde{C_v}(T) + \int_{v^0}^{v} \left(\frac{\partial C_v}{\partial v}\right)_T dv \qquad \text{(A-13)}$$

According to Van Wylen [45] , in a pure substance, derivative of specific heat with respect to the specific volume for constant temperature is given by:

$$\left(\frac{\partial C_v}{\partial v}\right)_T = T\left(\frac{\partial^2 P}{\partial T^2}\right)_v \qquad \text{(A-14)}$$

After substituting equation *(A-14*) to *(A-13*) , the specific heat at constant volume at temperature T and specific volume,v, is written as:

$$C_v(T,v) = \widetilde{C_v}(T) + \int_{v^0}^{v} T\left(\frac{\partial^2 P}{\partial T^2}\right)_v dv = \widetilde{C_v}(T) + \int_{v^0}^{v} T f_{TT} dv \qquad \text{(A-15)}$$

According to Van Wylen [45] , relation between specific heat at constant volume and the specific heat at constant pressure in a pure substance is given by:

$$C_P(T,v) - C_v(T,v) = -T\left(\frac{\partial v}{\partial T}\right)_P^2 \left(\frac{\partial P}{\partial v}\right)_T = -T\left(\frac{\partial P}{\partial T}\right)_v^2 \Big/ \left(\frac{\partial P}{\partial v}\right)_T \qquad \text{(A-16)}$$

This can be rearranged into the following form to calculate the specific heat at constant pressure:

$$C_P(T,v) = C_v(T,v) - T\frac{{f_T}^2(T,v)}{f_v(T,v)} \qquad \text{(A-17)}$$

A.2.2 Speed of Sound

The sound velocity in a pure substance is given by Van Wylen [45]:

$$\mathrm{a} = \sqrt{\left(\frac{\partial P}{\partial \rho}\right)_s} = \sqrt{-v^2\left(\frac{\partial P}{\partial v}\right)_s} = \sqrt{-v^2\frac{\left(\frac{\partial T}{\partial v}\right)_s}{\left(\frac{\partial T}{\partial P}\right)_s}} \qquad \text{(A-18)}$$

The isentropic derivatives in equation *(A-18)* can be replaced with the equivalent forms in equations *(A-9)* and *(A-10)*, which leads to the following equation:

$$\mathrm{a} = \sqrt{v^2\frac{C_p\left(\frac{\partial P}{\partial T}\right)_v}{C_v\left(\frac{\partial v}{\partial T}\right)_P}} = \sqrt{-v^2\frac{C_p}{C_v}\left(\frac{\partial P}{\partial v}\right)_T} \qquad \text{(A-19)}$$

Speed of sound ultimately is presented by:

$$\mathrm{a}(T, v) = \sqrt{-v^2\frac{C_p}{C_v}f_v(T, v)} \qquad \text{(A-20)}$$

A.2.3 Internal Energy

Thermodynamic relation between changes in temperature and specific volume and the changes in internal energy can be written as [45] :

$$\mathrm{d}i = C_v dT + \left[T\left(\frac{\partial P}{\partial T}\right)_v - P\right]dv \qquad \text{(A-21)}$$

The internal energy at temperature T and specific volume of,v , is obtained by two successive processes:

The first process occurs at constant pressure of $P = 0.1\ MPa$ and hydrogen is considered as an ideal gas at this stage. Temperature of hydrogen increases from $0^0 K$ to final temperature of T. Internal energy of hydrogen is zero at temperature of $T = 0^0 K$.

In this process, the second term in the *(A-21)* is zero and the increase in internal energy can be obtained by:

$$\Delta i_1 = \int_0^T \widetilde{C_v}(T) dT \qquad (A\text{-}22)$$

Specific volume of hydrogen at the end of the first process is equal to v^0, which is given by equation *(A-12)*.

In the second process, the specific volume of hydrogen changed from v^0 to the final value of v. Temperature is constant during this process and corresponding changes in the internal energy is calculated by:

$$\Delta i_2 = \int_{v^0}^{v} \left[T \left(\frac{\partial P}{\partial T} \right)_v - P \right] dv \qquad (A\text{-}23)$$

Combining the two processes which is formulated with equations (*A-22*) and *(A-23*) , changes in internal energy for a real gas is as follows:

$$\mathrm{i}(T, v) = \int_0^T \widetilde{C_v}(T) dT + \int_{v^0}^{v} [T f_T(T, v) - f(T, v)]\ dv \qquad (A\text{-}24)$$

the enthalpy is given as:

$$h(T, v) = i(T, v) + v f(T, v) \qquad (A\text{-}25)$$

A.2.4 Isentropic Expansion

The flow is expanded from the stagnation state inside the chamber to the sonic state at the throat. This expansion is considered as isentropic expansion and the flow properties of the isentropically expanded flow is calculated by integrating the ordinary differential equation of *(A-9*) with respect to the specific volume.

$$\mathrm{d}T = -\frac{T\, f_T(T,v)}{c_v(T,v)}\, dv \qquad \text{(A-26)}$$

Thermodynamic states which hydrogen goes through during the isentropic expansion, is determined by integration of equation *(A-26*).

The sonic state of the flow at the throat is the state which the following balance is satisfied:

$$\mathrm{i}(T_t, v_t) + v_t\, f(T_t, v_t) = i(T_n, v_n) + v_n f(T_n, v_n) + \frac{1}{2} a^2(T_n, v_n) \qquad \text{(A-27)}$$

A.3 Code Development

The analytical code is developed to calculate time histories of stagnation properties inside the chamber and sonic properties at the throat. The code is based on the equations, developed in the previous sections.

The release process of the high-pressure hydrogen, consist of two major and main steps:

- Isentropic expansion
- Adiabatic release

The algorithm which the computer code is developed and based on, is provided in Figure A-1.

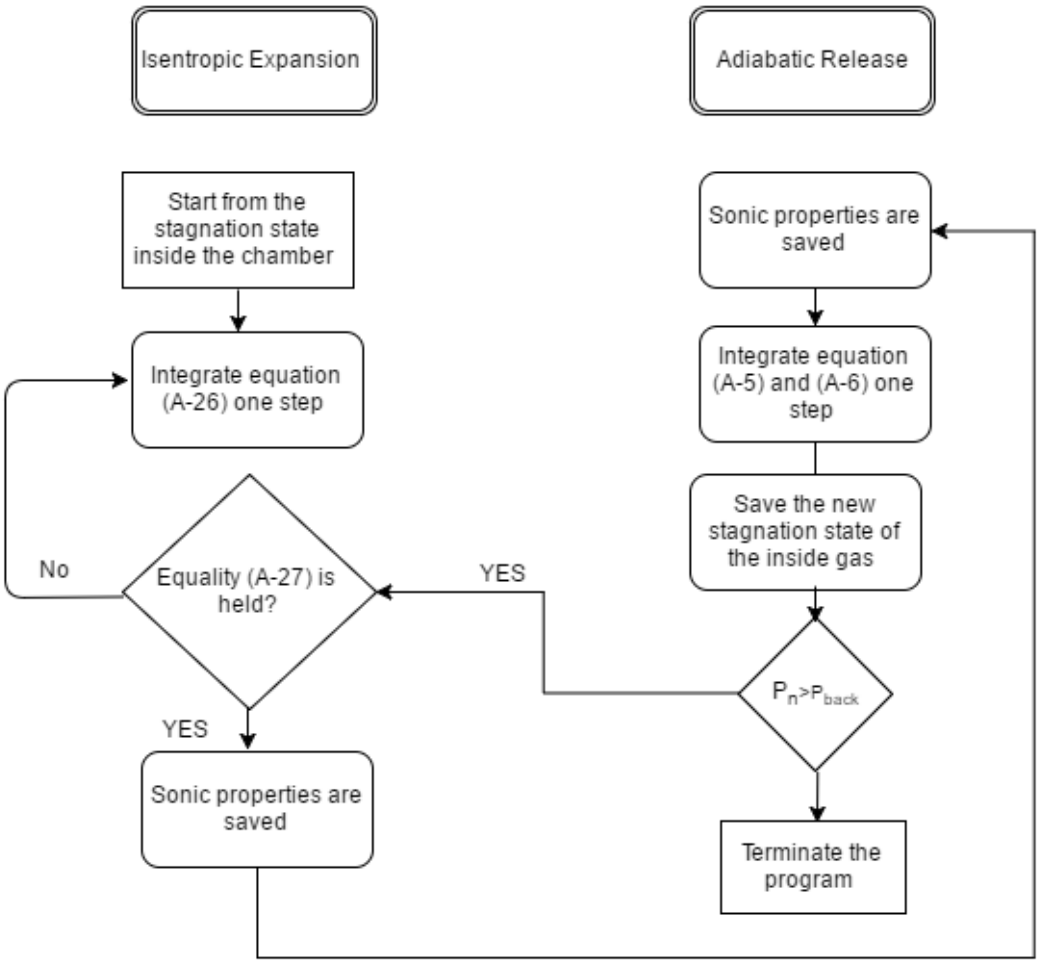

Figure A-1: Analytical code development algorithm

A.3.1 Isentropic Expansion

This step, involves numerical integration of equation *(A-26)* , to obtain the properties of the isentropically expanded flow. The initial condition is the stagnation state inside the chamber. Integration is performed using first order Euler method and the integration step is 0.05% of the stagnation specific volume. After each integration and each time step, the equality of *(A-27)* is evaluated to be satisfied. If the equality is satisfied, the most recently computed properties are the sonic properties at the throat.

A.3.2 Adiabatic Release

In this stage, the conservation of mass and energy equations are integrated to get the new stagnation state inside the chamber. First order Euler method with a time step of $10^{-6}\,Second$, is used to integrate the conservation equations. Integration of these equations results in internal energy and specific volume of the new stagnation state.

To obtain corresponding temperature of this new state, iterative approach is utilized. Secant iterative method is used to solve this equation *(A-24)*. By having the two independent properties of temperature and specific volume, pressure and other properties of the flow can be calculated.

APPENDIX B

FLOW EVOLUTION: FLOW PROPERTIES CONTOUR AT DIFFERENT TIMES OF RELEASE

In Figure B-1 to Figure B-4 flow development is illustrated by presenting flow properties contours at diff rent times of hydrogen release. The results correspond to the hydrogen storage tank with initial tank pressure of $P_0 = 10$ MPa and $T_0 = 300$ k .

- **Mass concentration contours**

T=5μs	T=10μs
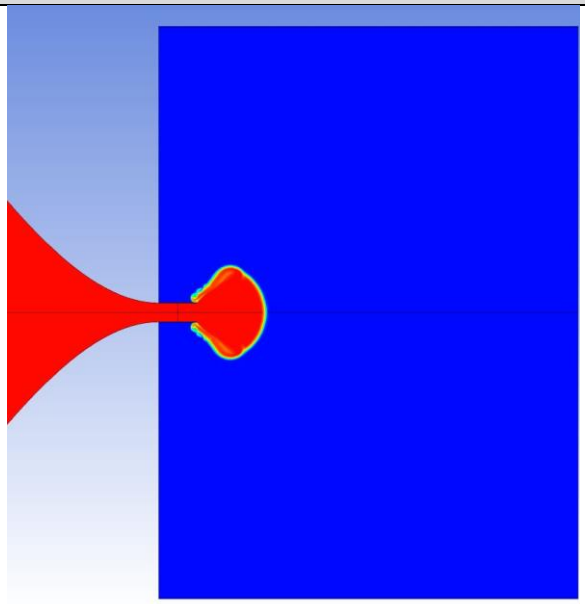	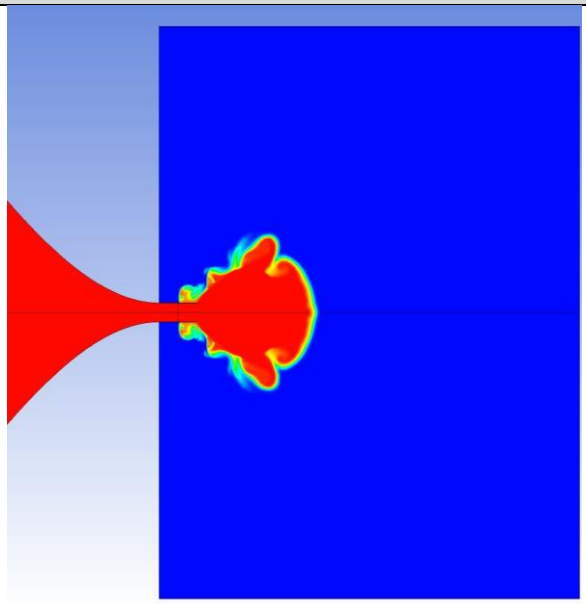
T=15μ	T=20μ
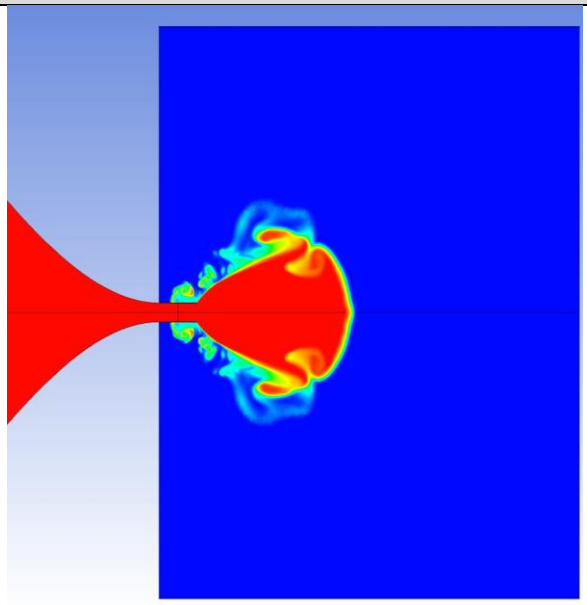	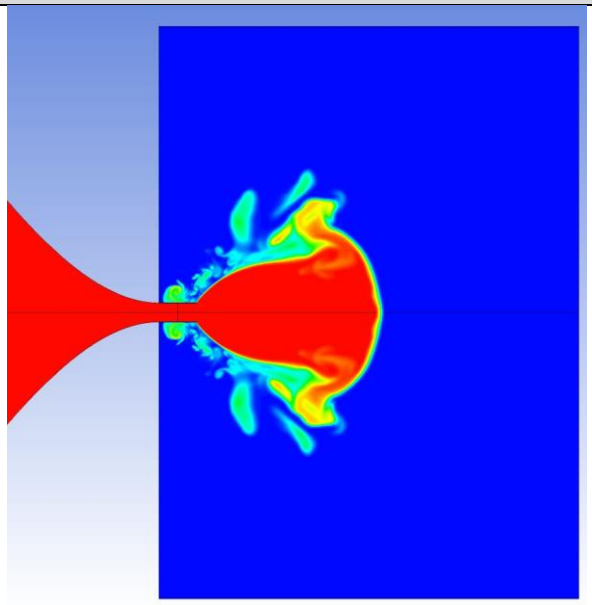

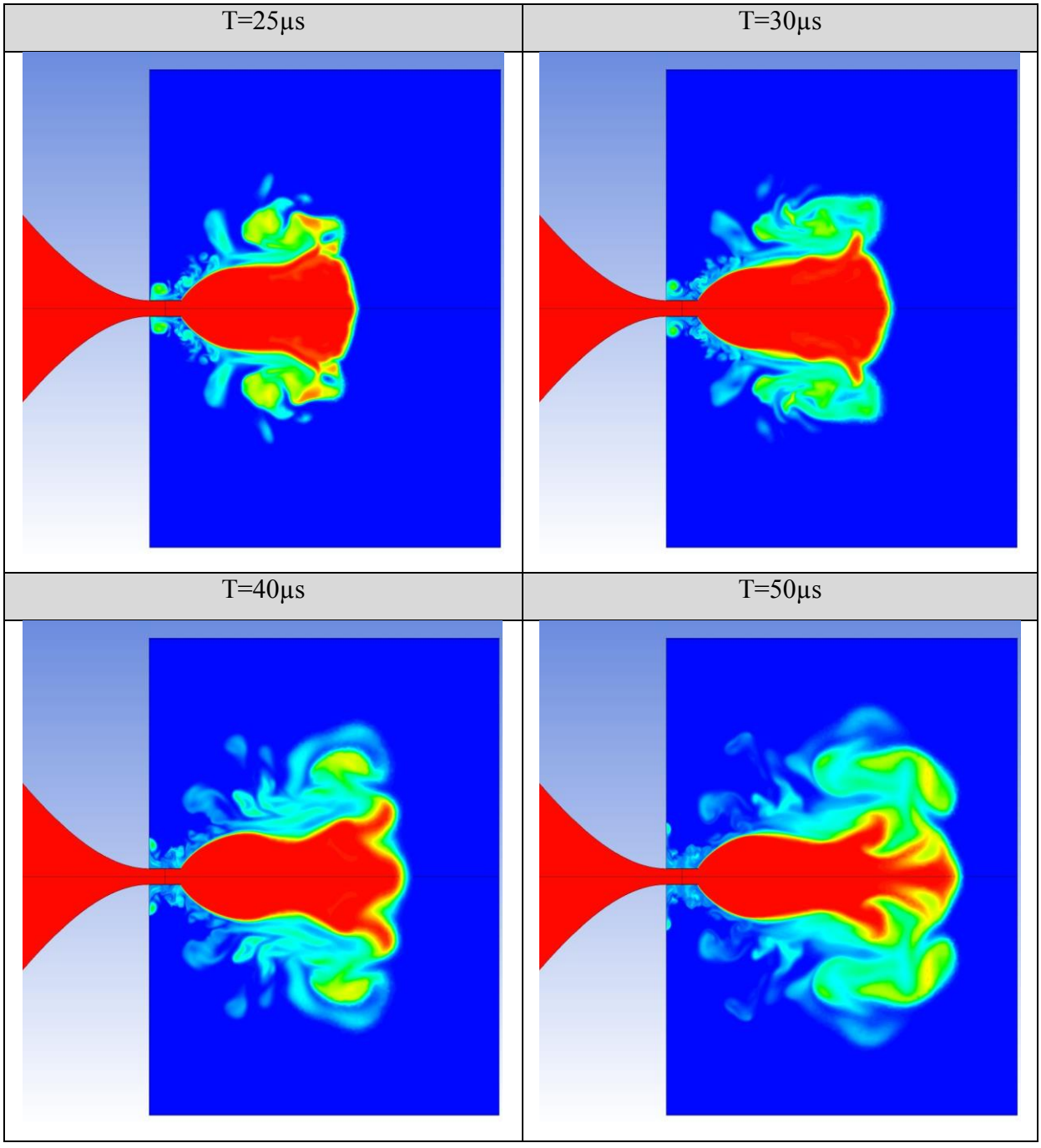

Figure B-1 : Mass concentration contour at different times of hydrogen release

- **Density contours**

T=5μs	T=10μs
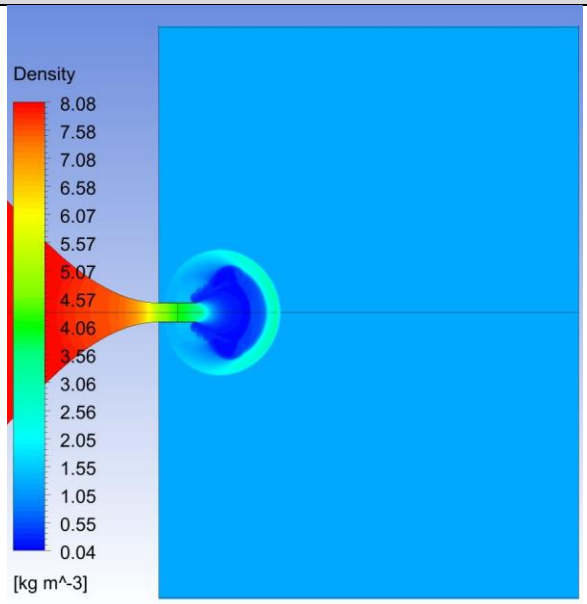	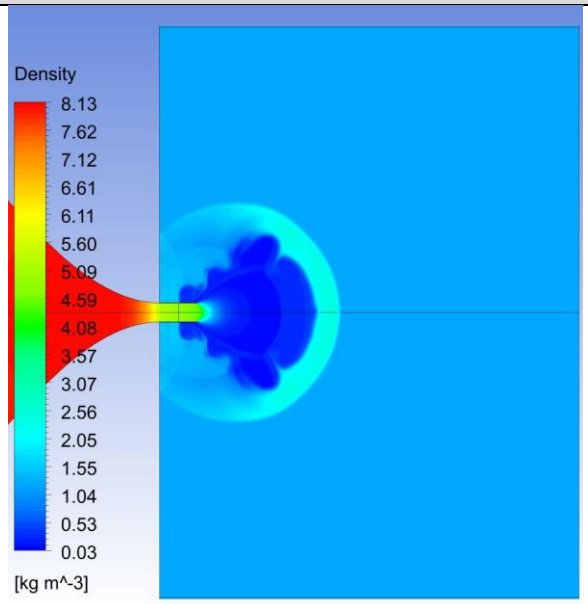
T=15μ	**T=20μ**
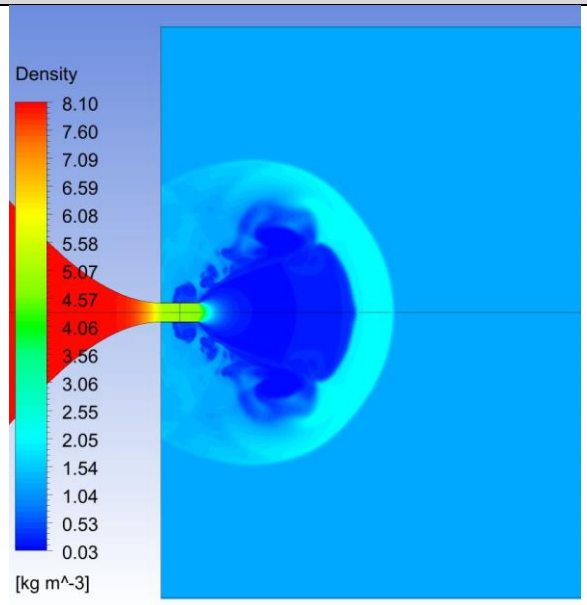	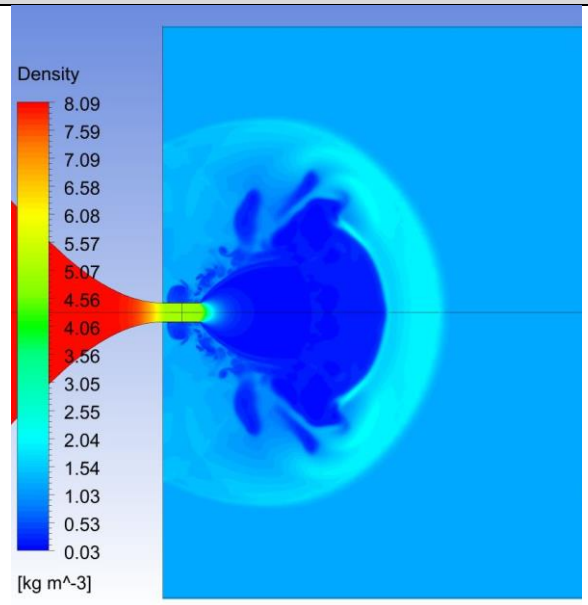

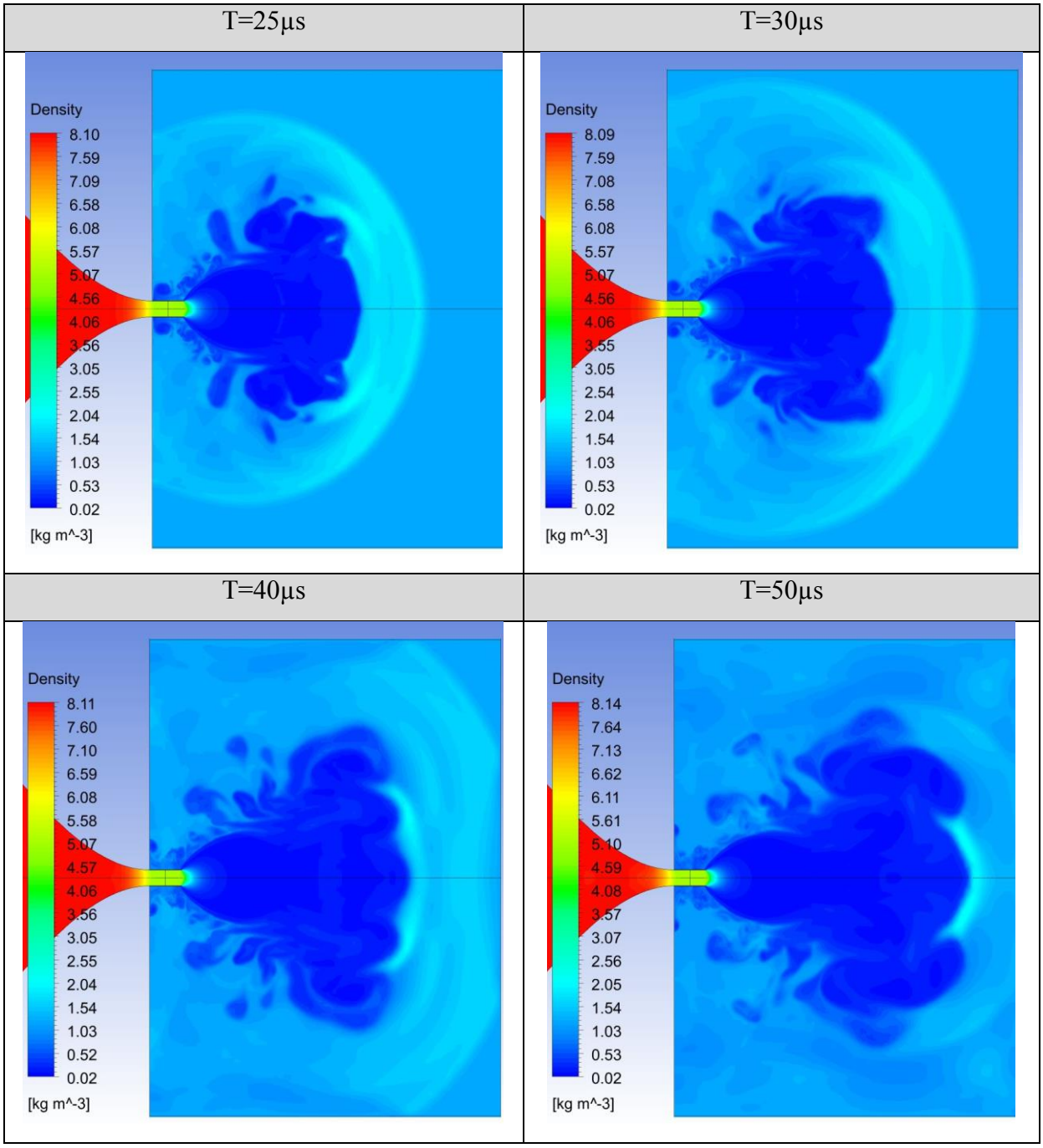

Figure B-2: Th flo density contour at different times of hydrogen release

- **Mach number contours**

T=5μs	T=10μs
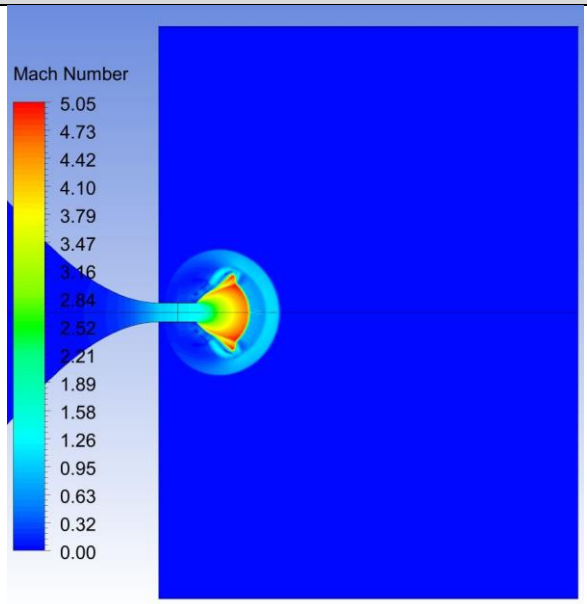	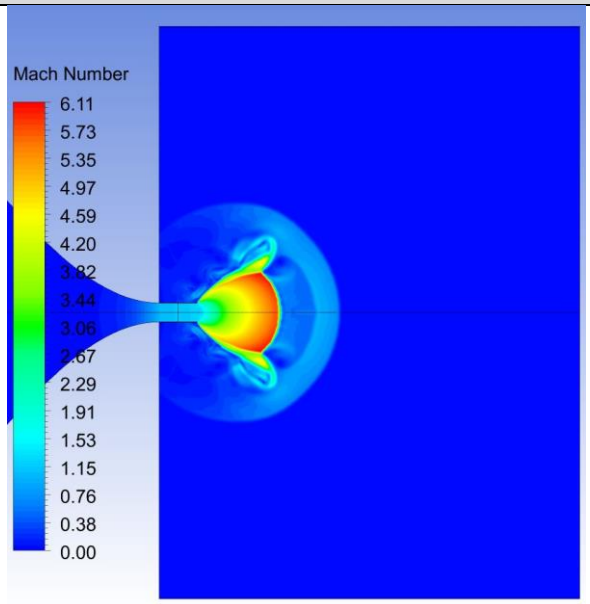
T=15μ	T=20μ
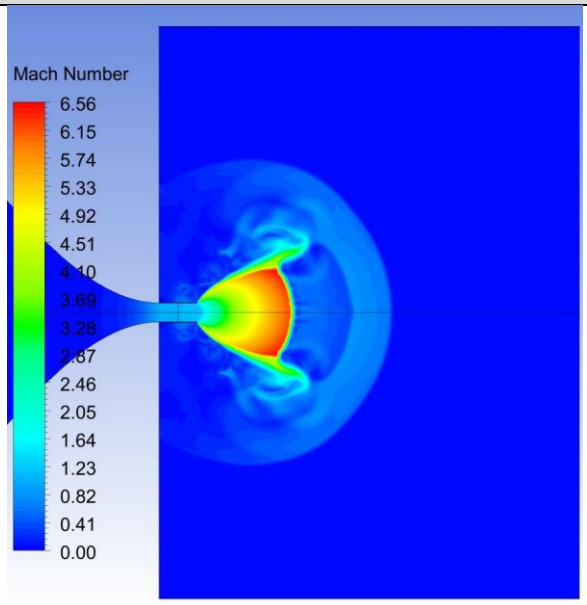	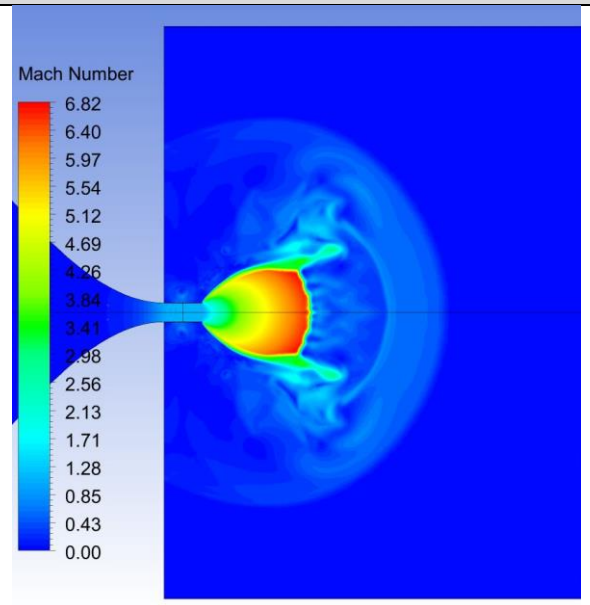

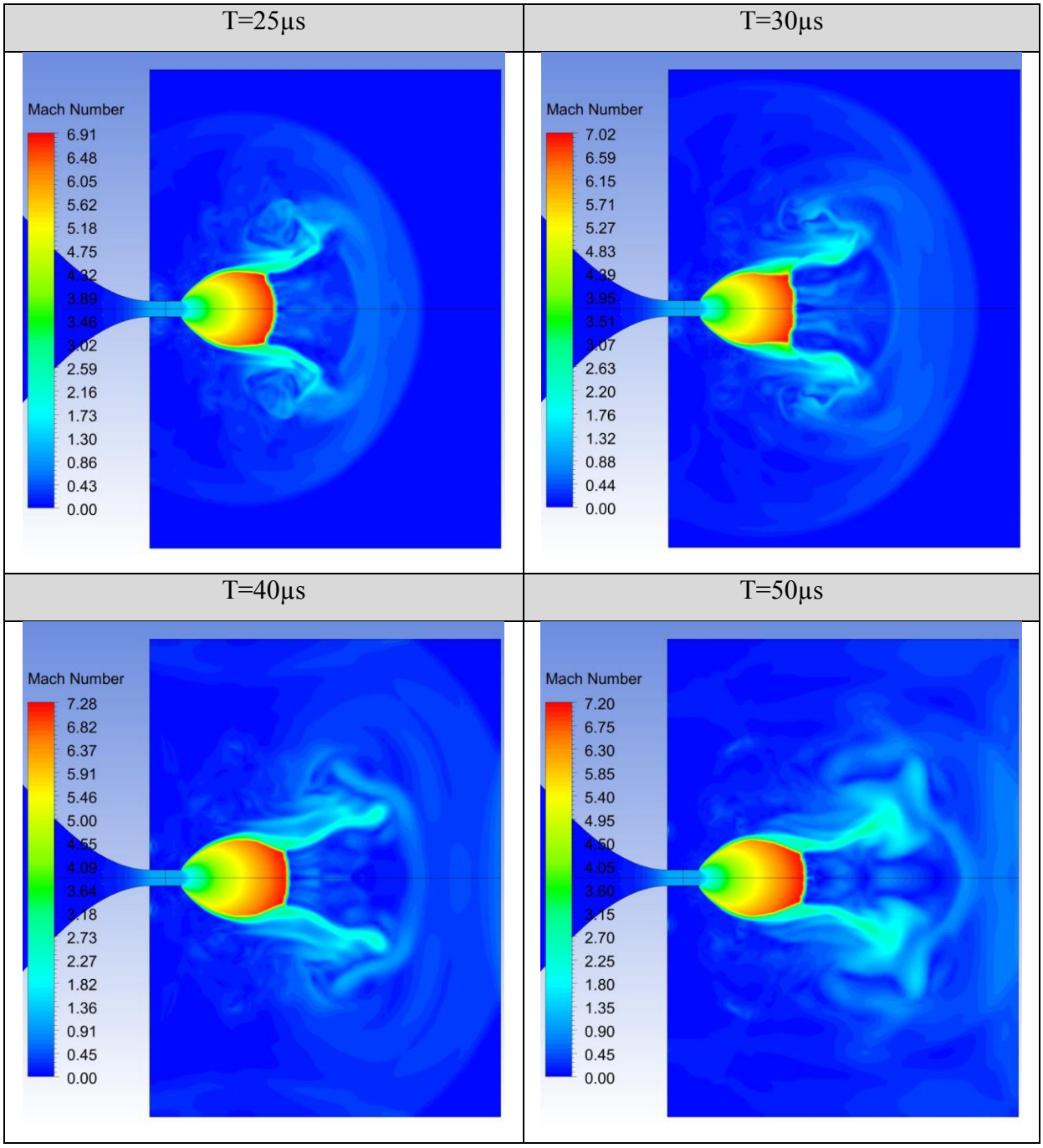

Figure B-3: Th flo Mach number contour at different times of hydrogen release

- **Flow temperature contours**

T=5μs	T=10μs
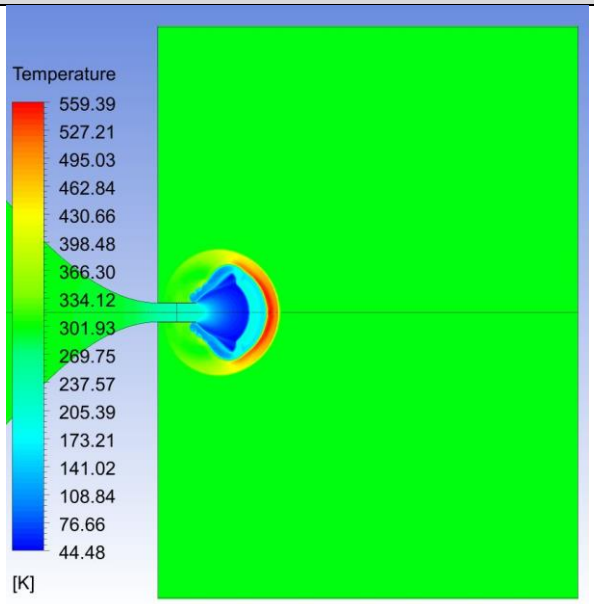	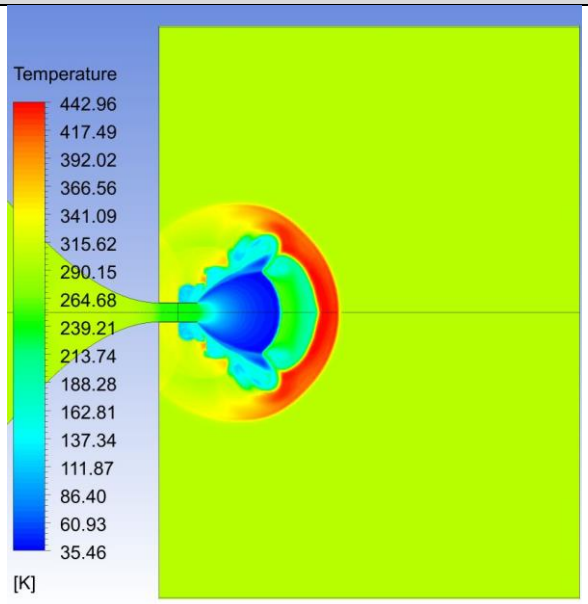
T=15μ	T=20μ
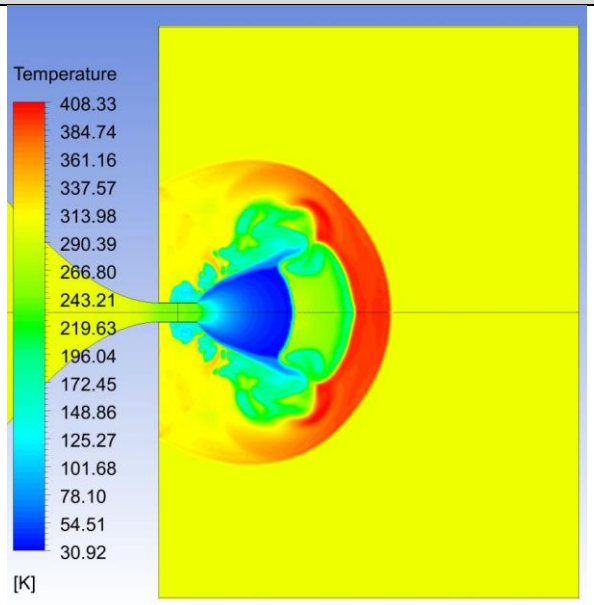	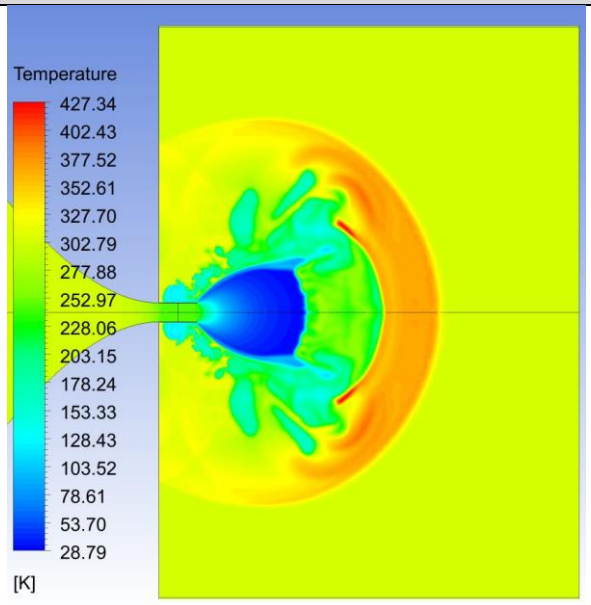

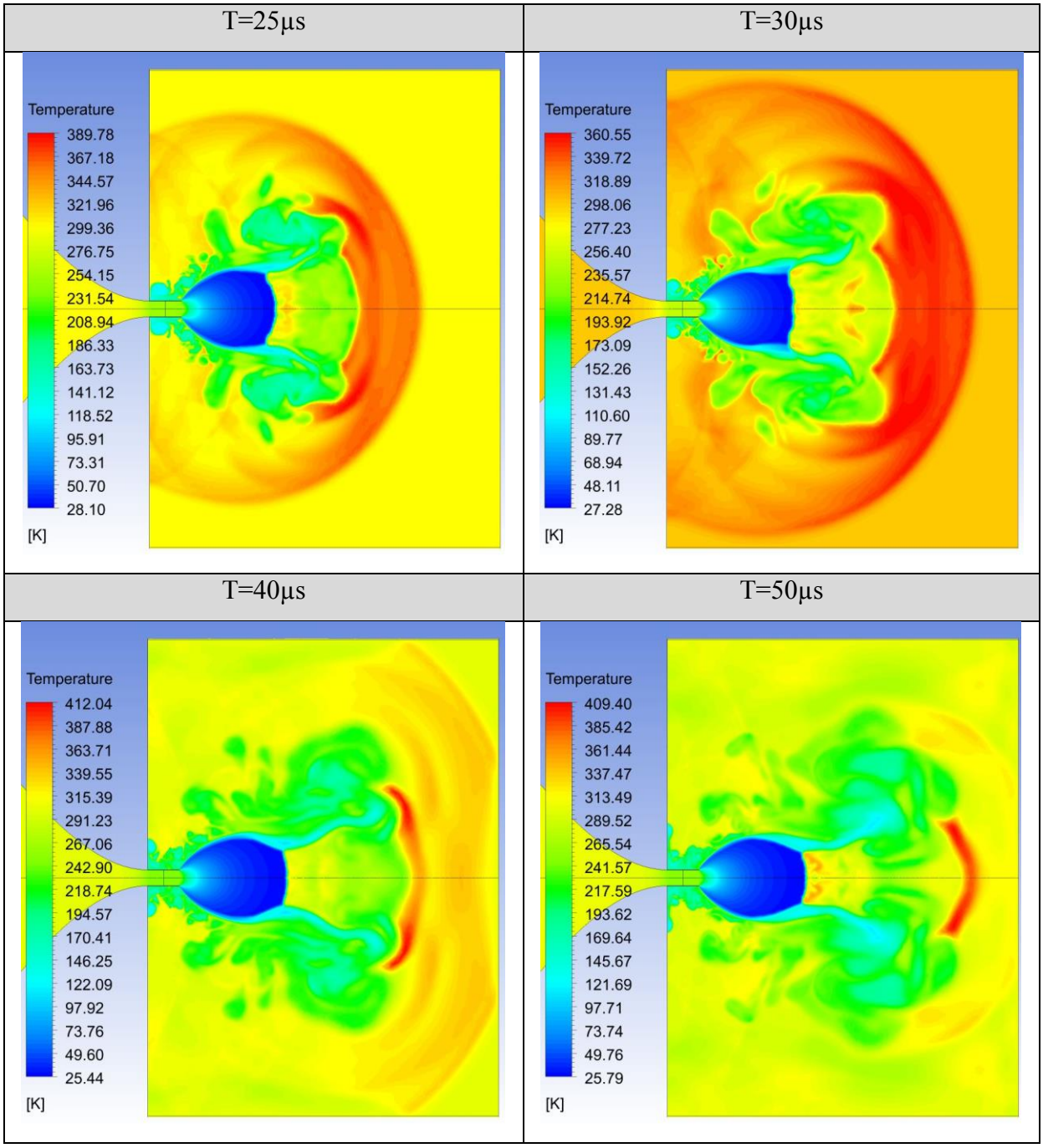

Figure B-4: Th flo temperature contour at different times of hydrogen release

APPENDIX C

FLOW EVOLUTION: FLOW PROPERTIES ALONG THE CENTERLINE

Figure C-1 to Figure C-4 show distribution of the flow properties along the centerline at diff rent times of hydrogen release from a reservoir with initial tank pressure of $P_0 = 10\ MPa$.

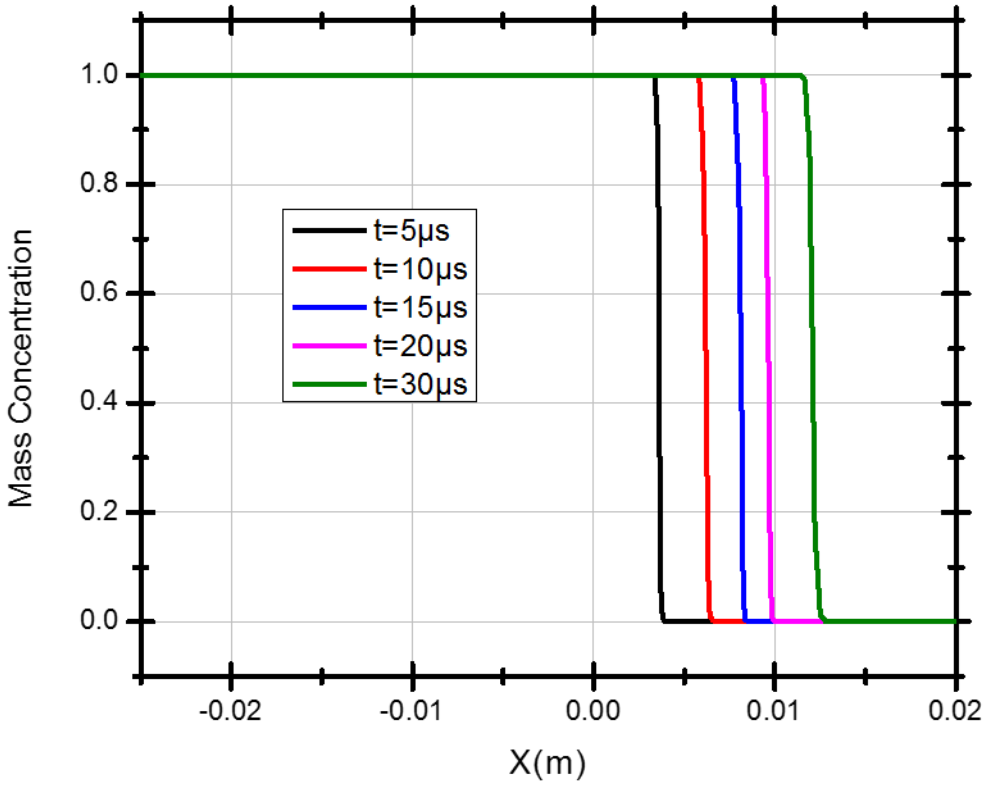

Figure C-1: Mass concentration distribution along the centerline at different times of release

The flow evolution is illustrated in Figure C-1, by means of providing flow mass concentration along the centerline. The mass concentration of unity signifies pure hydrogen and the mass

concentration of zero shows pure air. The flow is developed over time and the contact surface of hydrogen and air moves further downstream.

The flow Mach number distribution along the centerline are plotted in Figure C-2. The Mach disk advances through the atmospheric air by time. The maximum Mach number along the centerline increases and the Mach disk become stronger.

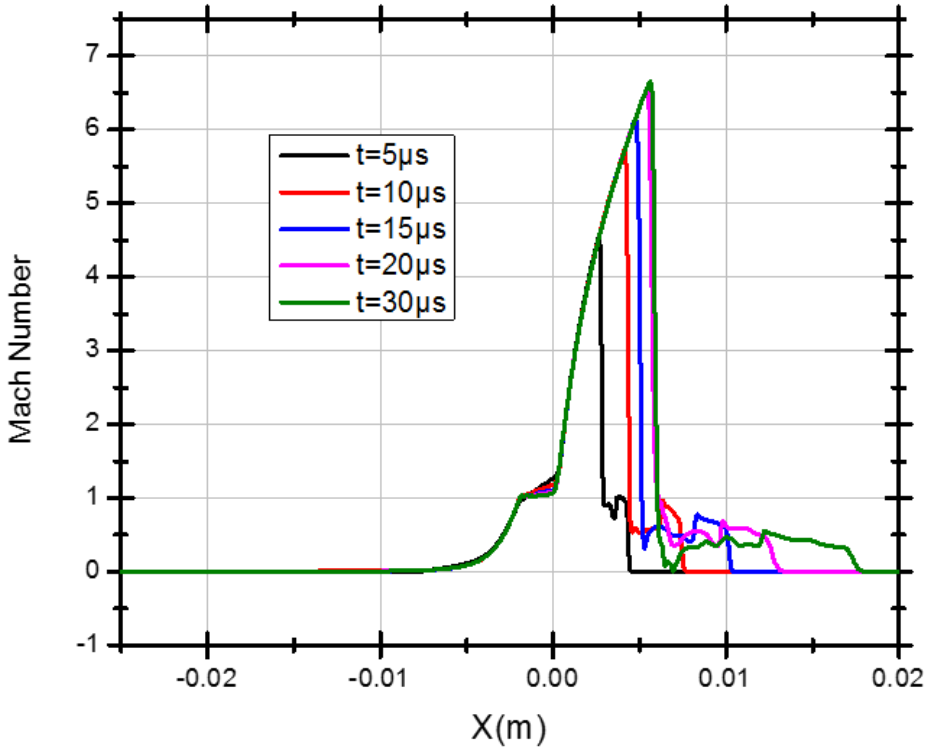

Figure C-2: Mach number distribution along the centerline at different times of release

The flow density distribution along the centerline is shown in Figure C-3. The flow density is low, upstream of the contact surface where the flow is pure hydrogen. The flow has higher density downstream of the contact surface. The maximum density downstream of the release area, occurs at the contact surface and this maximum density decrease over time.

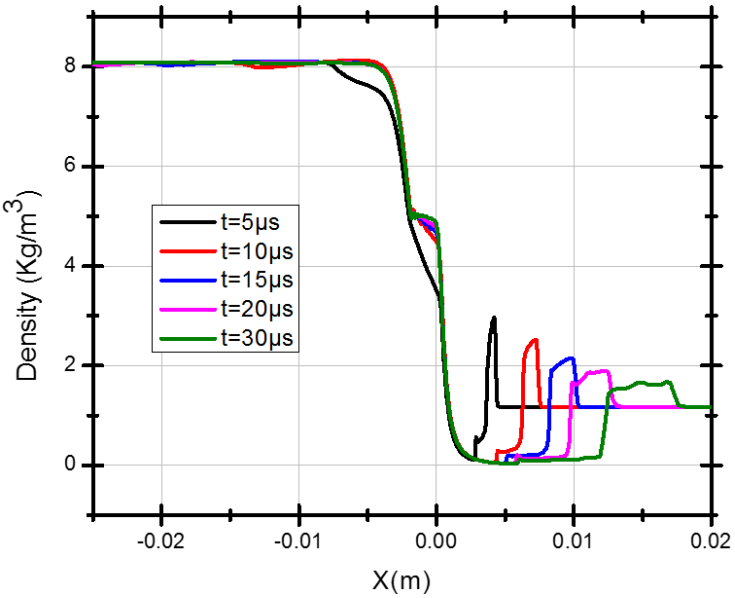

Figure C-3: Density distribution along the centerline at different times of release

The flow temperature distribution along the centerline is plotted in Figure C-4.

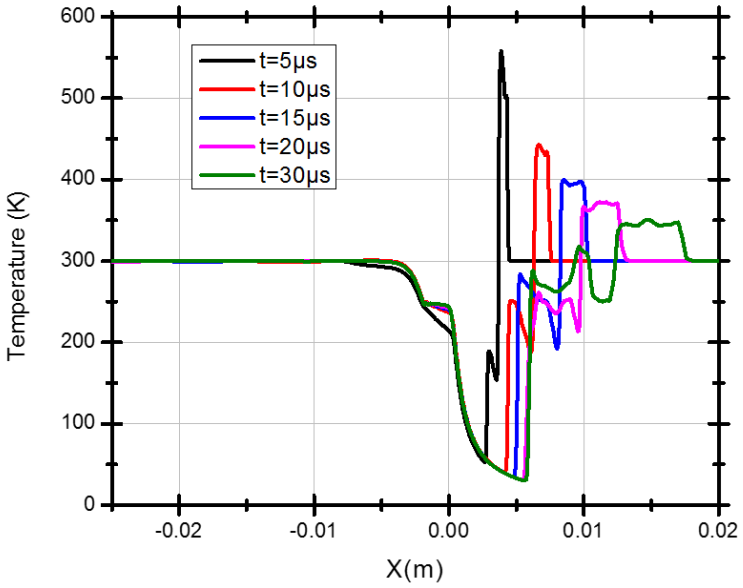

Figure C-4: Temperature distribution along the centerline at different times of hydrogen release

The maximum temperature occurs at the weak shock, ahead of the flow, where hydrogen concentration is zero. The weak shock increases the air temperature and the flow reaches its maximum temperature. The flow maximum temperature decreases by time during the hydrogen release.